Article

A temperate Earth-sized planet with tidal heating transiting an M6 star

Merrin S. Peterson[1], Björn Benneke[1✉], Karen Collins[2], Caroline Piaulet[1], Ian J. M. Crossfield[3], Mohamad Ali-Dib[1,4], Jessie L. Christiansen[5], Jonathan Gagné[6], Jackie Faherty[7], Edwin Kite[8], Courtney Dressing[9], David Charbonneau[2], Felipe Murgas[10], Marion Cointepas[11], Jose Manuel Almenara[11], Xavier Bonfils[11], Stephen Kane[12], Michael W. Werner[13], Varoujan Gorjian[13], Pierre-Alexis Roy[1], Avi Shporer[14], Francisco J. Pozuelos[15,16], Quentin Jay Socia[17], Ryan Cloutier[2,18], Jeremy Dietrich[17], Jonathan Irwin[2], Lauren Weiss[19], William Waalkes[20], Zach Berta-Thomson[20], Thomas Evans[14], Daniel Apai[17,21], Hannu Parviainen[10], Enric Pallé[10], Norio Narita[10,22,23], Andrew W. Howard[24], Diana Dragomir[25], Khalid Barkaoui[16,26], Michaël Gillon[16], Emmanuel Jehin[27], Elsa Ducrot[16], Zouhair Benkhaldoun[26], Akihiko Fukui[10,22], Mayuko Mori[28], Taku Nishiumi[23,29,30], Kiyoe Kawauchi[10,30], George Ricker[14], David W. Latham[2], Joshua N. Winn[31], Sara Seager[14,32,33], Howard Isaacson[9], Alex Bixel[17], Aidan Gibbs[34], Jon M. Jenkins[35], Jeffrey C. Smith[36], Jose Perez Chavez[37], Benjamin V. Rackham[14], Thomas Henning[38], Paul Gabor[39], Wen-Ping Chen[40], Nestor Espinoza[41], Eric L. N. Jensen[42], Kevin I. Collins[43], Richard P. Schwarz[2], Dennis M. Conti[44], Gavin Wang[45], John F. Kielkopf[46], Shude Mao[47], Keith Horne[48], Ramotholo Sefako[49], Samuel N. Quinn[2], Dan Moldovan[50], Michael Fausnaugh[14], Gábor Fűűrész[14] & Thomas Barclay[51,52]

Temperate Earth-sized exoplanets around late-M dwarfs offer a rare opportunity to explore under which conditions planets can develop hospitable climate conditions. The small stellar radius amplifies the atmospheric transit signature, making even compact secondary atmospheres dominated by N_2 or CO_2 amenable to characterization with existing instrumentation[1]. Yet, despite large planet search efforts[2], detection of low-temperature Earth-sized planets around late-M dwarfs has remained rare and the TRAPPIST-1 system, a resonance chain of rocky planets with seemingly identical compositions, has not yet shown any evidence of volatiles in the system[3]. Here we report the discovery of a temperate Earth-sized planet orbiting the cool M6 dwarf LP 791-18. The newly discovered planet, LP 791-18d, has a radius of $1.03 \pm 0.04\ R_\oplus$ and an equilibrium temperature of 300–400 K, with the permanent night side plausibly allowing for water condensation. LP 791-18d is part of a coplanar system[4] and provides a so-far unique opportunity to investigate a temperate exo-Earth in a system with a sub-Neptune that retained its gas or volatile envelope. On the basis of observations of transit timing variations, we find a mass of $7.1 \pm 0.7\ M_\oplus$ for the sub-Neptune LP 791-18c and a mass of $0.9^{+0.5}_{-0.4}\ M_\oplus$ for the exo-Earth LP 791-18d. The gravitational interaction with the sub-Neptune prevents the complete circularization of LP 791-18d's orbit, resulting in continued tidal heating of LP 791-18d's interior and probably strong volcanic activity at the surface[5,6].

LP 791-18d was detected through 127 h of dedicated, near-continuous Spitzer observations of LP 791-18, one of the smallest stars known to host planets. LP 791-18 was previously known to host the hot super-Earth LP 791-18b on a 0.94-day orbit and the sub-Neptune LP 791-18c on a 4.99-day orbit, both discovered in June 2019 by the Transiting Exoplanet Survey Satellite (TESS)[4], but both without radial-velocity confirmation or mass measurements.

Two transits of the newly discovered LP 791-18d are clearly visible in the 127-hour-long Spitzer light curve (Fig. 1), in addition to transits of the previously known planets LP 791-18b and c. We subsequently confirmed LP 791-18d's ephemeris using ground-based telescopes and discovered that the new LP 791-18d opens the system to mass measurements through transit timing variations (TTVs). We therefore complemented our observations of this system with a large multi-year, multi-telescope transit campaign totalling 72 transit observations between 2019 and 2021 including 43 transits of the Earth-sized planet LP 791-18d and 29 transits of sub-Neptune LP 791-18c (Methods, Extended Data Tables 1 and 2 and Extended Data Fig. 1). Our detection of TTVs, further discussed below, confirms the planetary nature of the LP 791-18 transit events by evincing the mutual gravitational interaction between planets c and d.

Article
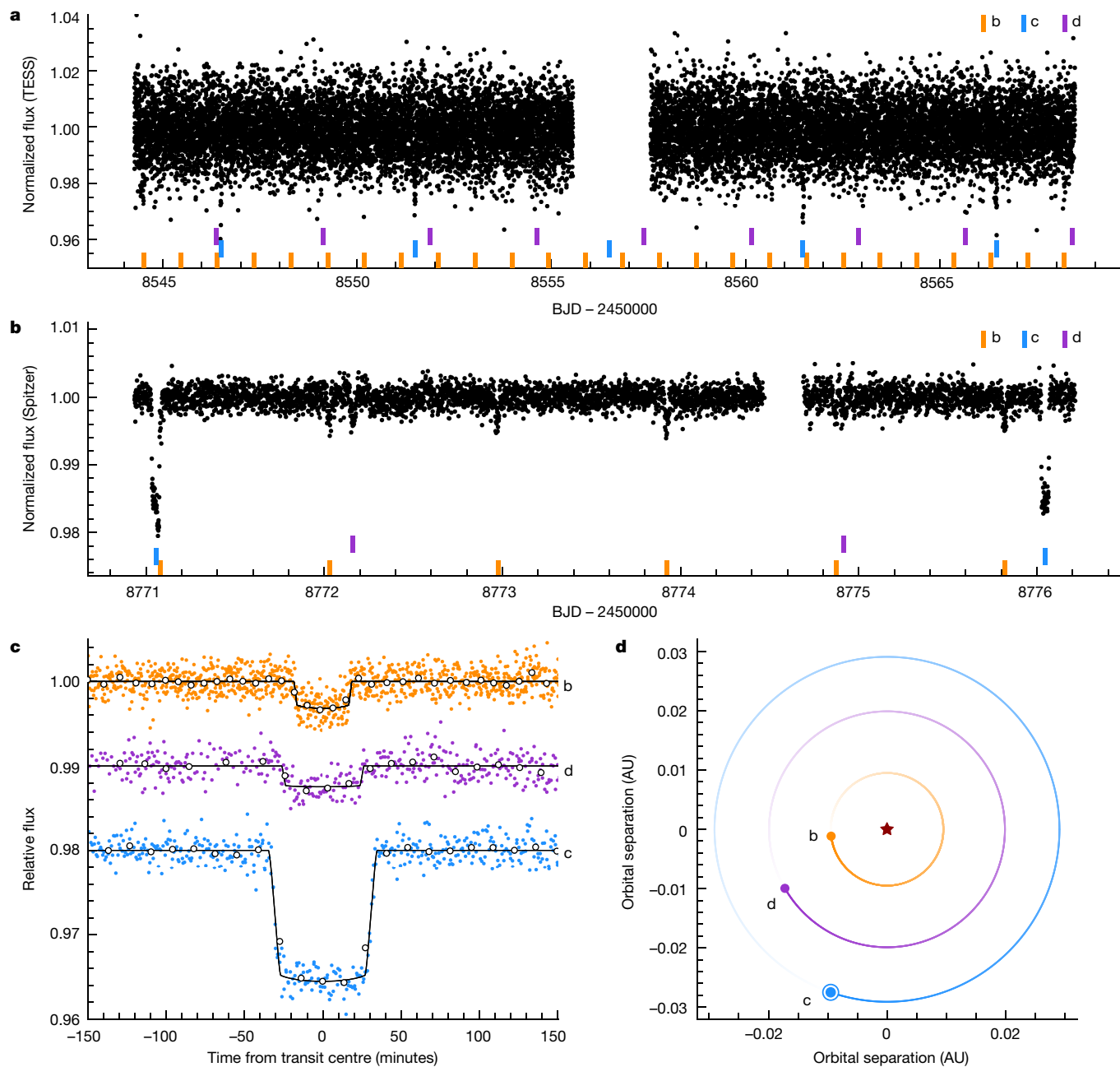
Fig. 1 | TESS and Spitzer light curves of LP 791-18. a, TESS observations of LP 791-18 taken between 1 and 25 March 2019 detrended using a Gaussian process with a fixed length scale of 1.0 days, with the transit times of planets b, c and d indicated. Only the transits of planet c are visible by eye. **b,c**, PLD-corrected and detrended Spitzer observations deliberately scheduled to capture two transits of planet c, with the first transit appearing much deeper due to overlap with the transit of planet b (**b**). The signatures of all three planets are visible by eye in the processed Spitzer data, and are also shown phase-folded in **c**. **d**, Snapshot of the orbits of the three planets.

The radius of the newly discovered LP 791-18d is consistent with that of the Earth ($1.03 \pm 0.04\ R_\oplus$) and its equilibrium temperature is 395 K for an Earth-like Bond albedo and 305 K for a Venus-like Bond albedo, assuming efficient heat redistribution around the planet. The orbital period of planet d is 2.753 days. In the analysis, we used a revised stellar luminosity ($0.00230 \pm 0.00001\ L_\odot$) and stellar radius ($0.182 \pm 0.007\ R_\odot$) based on a newly obtained Infrared Telescopy Facility (IRTF)–SpeX Prism spectrum and publicly available broadband measurements (Methods and Extended Data Table 3). We similarly refined the radius estimate of the sub-Neptune LP 791-18c to $2.44 \pm 0.10\ R_\oplus$ (Extended Data Table 4). Finally, we derived mass estimates by fitting the 72 mid-transit times of planets c and d using TTVFast transit timing modelling[7] in combination with emcee[8] (Methods).

TTVs with an amplitude of 4.53 ± 0.43 min are detected for LP 791-18d consistently in the Spitzer and ground-based observations (Fig. 2 and Extended Data Fig. 2). The TTVs constrain the mass of the sub-Neptune LP 791-18c to $7.1 \pm 0.7\ M_\oplus$ and the mass of the exo-Earth LP 791-18d to $0.9^{+0.5}_{-0.4}\ M_\oplus$ (Methods and Extended Data Table 4). Comparing the inferred radii and masses to planet interior models, we find that the mass of planet c is significantly below the $25\ M_\oplus$ that a purely rocky planet with the measured radius of planet c would have, indicating that planet c retained a significant amount of H_2/He envelope and/or a volatile-rich mantle. In interior model grids[9,10], a best match to the mass and radius is obtained for scenarios with $2.0^{+0.6}_{-0.5}\%$ of the planet's mass in a H_2/He envelope or, alternatively, roughly 50% of the entire planet composed of icy material (Extended Data Fig. 5). Either way, planet c
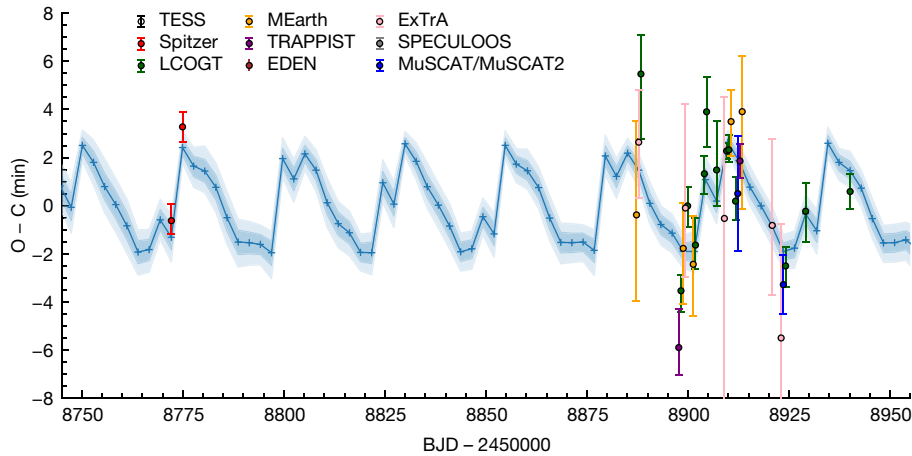
Fig. 2 | TTVs of LP 791-18d. Coloured data points indicate the transit timing measurements obtained with Spitzer (red), LCOGT (green), MuSCAT/MuSCAT2 (dark blue), MEarth (yellow), TRAPPIST (purple), EDEN (brown), ExTrA (pink) and SPECULOOS (grey), compared to the best-fitting TTVFast model (blue curve). The vertical axis represents the deviation from the best-fitting linear ephemeris and the horizontal axis the barycentric Julian date (BJD) of the observation. Dark and light shaded regions illustrate the posterior population of models in the MCMC fit corresponding to 68% and 95% confidence,

respectively. TTVs with 4.53 ± 0.43 min chopping amplitude are consistently detected in both the Spitzer and ground-based data, at a phase consistent with the planetary conjunctions of planets c and d. Some transits near BJD of 2458900 were observed with up to four telescopes simultaneously, with points slightly offset horizontally for clarity. Only part of the data set is shown here for clarity, and the full data set of 72 transit timing measurements of LP 791-18c and d is depicted in Extended Data Fig. 2.

must have been able to hold onto a substantial amount of volatiles or gas. The newly found planet LP 791-18d, on the other hand, is consistent with a rocky, potentially Earth-like, composition given its radius of $1.03 \pm 0.04\,R_\oplus$ and its mass of $0.9^{+0.5}_{-0.4}\,M_\oplus$. LP 791-18d is unlikely to harbour any hydrogen atmosphere today, as the maximum amount of hydrogen consistent with the observed planet radius would be unstable to atmospheric escape (Methods).

Together in the same system, the two planets span the small-planet radius valley and offer a rare opportunity to test planet formation and gas envelope evolution models in the previously poorly explored regime of late-M dwarfs. Well-established for FGK-type stars[11], recent planet demographics studies of early-to-mid M stars have suggested a similar dearth of planets[12], with some suggesting that gas-poor planet formation[13], rather than photoevaporation[14] or core-powered mass loss[15], may dominate the evolution of planets around low-mass stars[12]. LP 791-18 being the only known late-M-dwarf system with planets spanning the radius valley, we begin to put this hypothesis to the test for late-M dwarfs. We find longer mass-loss timescales for the sub-Neptune LP 791-18c, when compared to LP 791-18d, consistent with the predictions from photoevaporation[16] and core-powered mass loss[15,17] (Methods and Extended Data Fig. 6). We conclude that both thermally driven mass loss as well as gas-poor formation remain viable formation scenarios for LP 791-18d.

Depending on its formation history, LP 791-18d can therefore host a wide range of plausible atmospheres and amounts of volatiles at its surface. If the core of LP 791-18d had already formed before disc dissipation, LP 791-18d could have captured an early hydrogen-rich atmosphere shortly after formation, similar to the sub-Neptune LP 791-18c orbiting just exterior to LP 791-18d's orbit. Whereas it was probably short-lived on LP 791-18d (Methods), this hydrogen-rich atmosphere could have triggered magma mantle–atmospheric interactions, possible resulting in the formation of many Earth-oceans worth of H_2O by means of H_2 oxidization by $Fe^{2+}O$ in the mantle[18]. A large fraction of this H_2O could have safely been harboured in the planet's interior during the magma ocean phase and would then have outgassed only gradually over geological timescales. In this gas-rich formation scenario, the result could be a highly oxygen-rich, low carbon-to-oxygen ratio, endogenous water world with the total amount of water in the envelope and mantle depending on the intitial FeO content of the
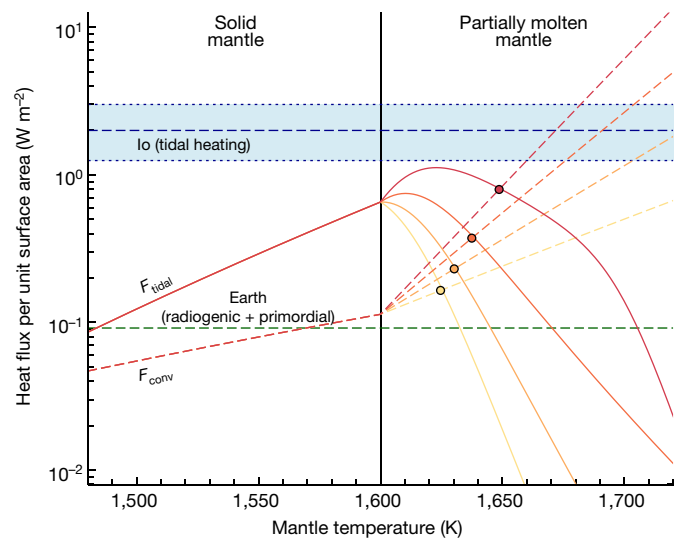

Fig. 3 | Internal energy balance of LP 791-18d in the presence of tidal heating. Coloured curves trace the tidal heating per unit surface area $F_{\text{tidal}} = \dot{E}_{\text{tidal}}/4\pi R^2$ (solid) and the convective heat transport towards the surface F_{conv} (dashed) as a function of the mantle temperature for the inferred forced eccentricity of LP 791-18d ($e = 0.0015$). The equilibrium mantle temperature is reached where $F_{\text{tidal}} = F_{\text{conv}}$ (coloured circles). Four sets of curves and equilibrium points are shown across the full range of melt fraction coefficients, with $B = 10$ shown in yellow, $B = 20$ in light orange, $B = 30$ in dark orange and $B = 40$ in red (Methods). In all cases, as the planet cooled down, equilibrium was reached beyond the solidus temperature (vertical black line), indicating that LP 791-18d has a partially molten mantle due to tidal heating. The surface flux due to tidal heating is 0.2–0.9 W m^{-2} and, therefore, up to an order of magnitude stronger than Earth's surface heat flux of 0.0916 W m^{-2} due to radioactive decay and primordial heat[24], probably dominating the internal heat flux budget of LP 791-18d. Strong volcanism, surface eruptions and atmospheric replenishment exceeding those of Earth would be the likely result. For another comparison, the range of inferred heat flux estimates for Jupiter's moon Io, the most geologically active body in the Solar System, is shown in blue, with the horizontal blue dotted lines indicating the lowest and highest estimates in the literature[25].
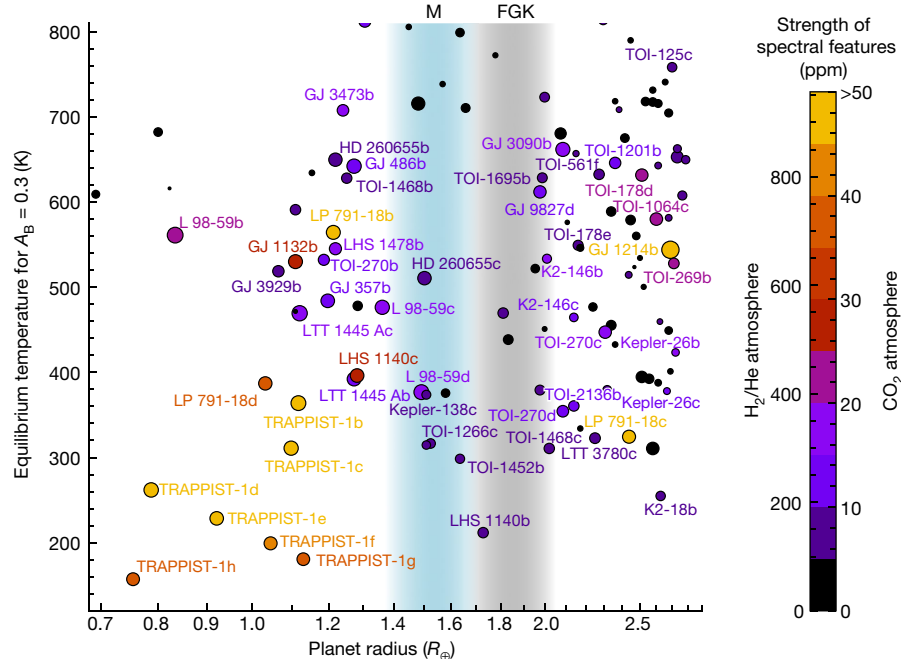
Fig. 4 | Temperature and radius of small transiting planets with measured masses amenable to transit spectroscopy. Colours indicate the expected strength of spectral features introduced by a CO_2-dominated atmosphere (five scale heights; right labels on colour bar), whereas point sizes indicate the relative SNR achievable per transit in the photon-noise limit, akin to the Transit Spectroscopy Metric[26]. For rocky planets, both quantities (colour and marker size) are essential in determining whether a planet is a good target for atmospheric characterization due to the separate limits introduced by photon noise and a potential systematic noise floor[27–29]. All planets with expected atmospheric signals greater than 7 ppm for CO_2 atmospheres are labelled by name, albeit many of them would require transit depth precision of only a few ppm for significant molecular detections (purple labels). Small planets

orbiting LP 791-18 and TRAPPIST-1 (yellow, orange) are unique in terms of the strength of their atmospheric signatures as well as their number of transit events per year. LP 791-18 and TRAPPIST-1 also offer the advantage that they can be observed with the JWST–Near Infared Spectrograph prism without saturation to simultaneously obtain 0.6–5.3 μm. The diffuse vertical stripes near 1.4–1.7 $R_\oplus$ (light blue) and 1.7–2.0 $R_\oplus$ (grey) highlight the locations of the radius valleys for M stars[12] and FGK stars[11], respectively. Note that planets that host H_2/He-rich atmospheres can show substantially stronger spectral features due to their larger scale heights (left labels on colour bar). Such atmospheres are believed to be more common for planets with radii beyond the radius valley[11,30]. Equilibrium temperatures are shown for a Bond albedo of $A_B = 0.3$ similar to Earth.

magma and the mass of hydrogen accreted during its early formation history[18]. Alternatively, if LP 791-18d formed as a gas-poor terrestrial planet without primordial gas envelope (gas-poor formation), then the planet could have formed a secondary atmosphere similar to Earth and Venus through outgassing or the accretion of volatile-rich solids. The composition of an outgassed atmosphere would then depend on the complex volatile exchange with the molten interior, governed by redox reactions and volatile solubilities during the magma ocean phase[19], and affected by the rate and tectonic setting of volcanism after the magma ocean phase.

The hypothesis of active ongoing outgassing on LP 791-18d is further strengthened by the inferred non-zero forced eccentricity of 0.0015 ± 0.00014 (11σ) resulting from the continued gravitational interaction with the eight times more massive LP 791-18c in near-resonance (Methods and Extended Data Figs. 3 and 4). This non-zero eccentricity introduces significant tidal heating of LP 791-18d's interior, with the resulting surface heat flux (0.2–0.9 W m^{-2}) up to an order of magnitude larger than the heat flux that Earth's surface experiences due to the radiogenic and primordial heat in Earth's interior (Fig. 3 and Methods). For a rocky surface composition, this would result in surface eruptions and volcanic activity, potentially similar to Jupiter's tidally heated moon Io[5,6], which in turn would continuously replenish the atmosphere of LP 791-18d with outgassed, potentially detectable, molecular species. In all modelled scenarios, we consider LP 791-18d in a tidally locked state (Methods) and we find mantle equilibrium temperatures above the solidus temperature of rock, indicating that the mantle of LP 791-18d can maintain a permanent molten silicate layer.

The tidally locked state of LP 791-18d also results in atmospheric dynamics and a climate pattern distinctively different from those of Venus and Earth, with the permanent day side receiving all the stellar insolation. Depending on the planet's yet-unknown evolutionary history, LP 791-18d may either have entered a Venus-like runaway greenhouse state[20,21] and possibly lost all its volatiles to space, or alternatively, LP 791-18d could have entered a 'collapsed' regime, in which water began to be captured in permanent cold traps on the night side or at the poles, thereby possibly avoiding the runaway and moist greenhouse regimes altogether[22,23] (Methods). Looking forwards, LP 791-18d, being a probably volcanically highly active Earth-sized planet near the inner edge of the habitable zone of a late-M dwarf in a system with a sub-Neptune offers several unprecedented opportunities to advance our understanding of the evolution of Earth-sized planets, the outgassing and atmospheric retention of temperate rocky planets in general, as well as the origin of the radius valley (Fig. 4 and Methods).

Online content

Any methods, additional references, Nature Portfolio reporting summaries, source data, extended data, supplementary information, acknowledgements, peer review information; details of author contributions and competing interests; and statements of data and code availability are available at https://doi.org/10.1038/s41586-023-05934-8.

1. Gillon, M. et al. The TRAPPIST-1 JWST Community Initiative. *Bull. AAS* https://doi.org/10.3847/25c2cfeb.afbf0205 (2020).
2. Gillon, M. Searching for red worlds. *Nat. Astron.* **2**, 344–344 (2018).

3. Agol, E. et al. Refining the transit-timing and photometric analysis of TRAPPIST-1: masses, radii, densities, dynamics, and ephemerides. *Planet. Sci. J.* **2**, 1 (2021).

4. Crossfield, I. J. M. et al. A super-Earth and sub-Neptune transiting the late-type M dwarf LP 791-18. *Astrophys. J.* **883**, L16 (2019).

5. Spencer, J. R. et al. Io's thermal emission from the Galileo photopolarimeter-radiometer. *Science* **288**, 1198–1201 (2000).

6. Veeder, G. J., Matson, D. L., Johnson, T. V., Davies, A. G. & Blaney, D. L. The polar contribution to the heat flow of Io. *Icarus* **169**, 264–270 (2004).

7. Deck, K. M., Agol, E., Holman, M. J. & Nesvorný, D. TTVFast: an efficient and accurate code for transit timing inversion problems. *Astrophys. J.* **787**, 132 (2014).

8. Foreman-Mackey, D., Hogg, D. W., Lang, D. & Goodman, J. Emcee: the MCMC hammer. *Publ. Astron. Soc. Pac.* **125**, 306–312 (2013).

9. Lopez, E. D. & Fortney, J. J. Understanding the mass-radius relation for sub-Neptunes: radius as a proxy for composition. *Astrophys. J.* **792**, 1 (2014).

10. Aguichine, A., Mousis, O., Deleuil, M. & Marcq, E. Mass–radius relationships for irradiated ocean planets. *Astrophys. J.* **914**, 84 (2021).

11. Fulton, B. J. & Petigura, E. A. The California-Kepler survey. VII. Precise planet radii leveraging Gaia DR2 reveal the stellar mass dependence of the planet radius gap. *Astron. J* **156**, 264 (2018).

12. Cloutier, R. & Menou, K. Evolution of the radius valley around low-mass stars from Kepler and K2. *Astron. J* **159**, 211 (2020).

13. Lee, E. J. & Connors, N. J. Primordial radius gap and potentially broad core mass distributions of super-earths and sub-Neptunes. *Astrophys. J.* **908**, 32 (2021).

14. Owen, J. E. & Wu, Y. The evaporation valley in the Kepler planets. *Astrophys. J.* **847**, 29 (2017).

15. Gupta, A. & Schlichting, H. E. Sculpting the valley in the radius distribution of small exoplanets as a by-product of planet formation: the core-powered mass-loss mechanism. *Mon. Not. R. Astron. Soc.* **487**, 24–33 (2019).

16. Owen, J. E. & Campos Estrada, B. Testing exoplanet evaporation with multitransiting systems. *Mon. Not. R. Astron.Soc.* **491**, 5287–5297 (2020).

17. Cloutier, R. et al. A pair of TESS planets spanning the radius valley around the nearby mid-M dwarf LTT 3780. *Astron. J.* **160**, 3 (2020).

18. Kite, E. S. & Schaefer, L. Water on hot rocky exoplanets. *Astrophys. J.* **909**, L22 (2021).

19. Bower, D. J., Hakim, K., Sossi, P. A. & Sanan, P. Retention of water in terrestrial magma oceans and carbon-rich early atmospheres. *Planet. Sci. J.* **3**, 93 (2022).

20. Kopparapu, R. K. in *Handbook of Exoplanets* (eds Deeg, H. J. & Belmonte, J. A.) 2981–2993 (Springer International Publishing, 2018).

21. Turbet, M. et al. Day–night cloud asymmetry prevents early oceans on Venus but not on Earth. *Nature* **598**, 276–280 (2021).

22. Leconte, J. et al. 3D climate modeling of close-in land planets: circulation patterns, climate moist bistability, and habitability. *Astron. Astrophys.* **554**, A69 (2013).

23. Wordsworth, R. D. Atmospheric nitrogen evolution on Earth and Venus. *Earth Planet. Sci. Lett.* **447**, 103–111 (2016).

24. Davies, J. H. & Davies, D. R. Earth's surface heat flux. *Solid Earth* **1**, 5–24 (2010).

25. Veeder, G. J. et al. Io: volcanic thermal sources and global heat flow. *Icarus* **219**, 701–722 (2012).

26. Kempton, E. M.-R. et al. A framework for prioritizing the TESS planetary candidates most amenable to atmospheric characterization. *Publ. Astron. Soc. Pac.* **130**, 114401 (2018).

27. Deming, D. et al. Discovery and characterization of transiting super earths using an all-sky transit survey and follow-up by the James Webb Space Telescope. *Publ. Astron. Soc. Pac.* **121**, 952–967 (2009).

28. Greene, T. P. et al. Characterizing transiting exoplanet atmospheres with JWST. *ApJ* **817**, 17 (2016).

29. Matsuo, T. et al. Photometric precision of a Si:As impurity band conduction mid-infrared detector and application to transit spectroscopy. *Publ. Astron. Soc. Pac.* **131**, 124502 (2019).

30. Benneke, B. et al. Water vapor and clouds on the habitable-zone sub-Neptune exoplanet K2-18b. *Astrophys. J. Lett.* **887**, L14 (2019).

[1]Department of Physics and Trottier Institute for Research on Exoplanets, Université de Montréal, Montreal, Quebec, Canada. [2]Center for Astrophysics, Harvard and Smithsonian, Cambridge, MA, USA. [3]Department of Physics and Astronomy, University of Kansas, Lawrence, KS, USA. [4]Center for Astro, Particle and Planetary Physics (CAP3), New York University Abu Dhabi, Abu Dhabi, United Arab Emirates. [5]Caltech/IPAC-NASA Exoplanet Science Institute, Pasadena, CA, USA. [6]Planetarium of Rio Tinto Alcan and Institute for Research on Exoplanets, University of Montréal, Montreal, Quebec, Canada. [7]American Museum for National History, New York, NY, USA. [8]Department of the Geological Sciences, University of Chicago, Chicago, IL, USA. [9]Department of Astronomy, University of California - Berkeley, Berkeley, CA, USA. [10]Instituto de Astrofísica de Canarias, La Laguna, Spain. [11]Institute of Planetology and Astrophysics of Grenoble, Grenoble, France. [12]Department of Earth and Planetary Sciences, University of California, Riverside, CA, USA. [13]Jet Propulsion Laboratory, California Institute of Technology, Pasadena, CA, USA. [14]Department of Physics and Kavli Institute of Astronomy, Massachusetts Institute of Technology, Cambridge, MA, USA. [15]Institute of Astrophysics of Andalucía (IAA-CSIC), Glorieta de la Astronomía s, Granada, Spain. [16]Astrobiology Research Unit, University of Liège, Liège, Belgium. [17]Steward Observatory, Tucson, AZ, USA. [18]Department of Physics and Astronomy, McMaster University, Ontario, Hamilton, Canada. [19]University of Hawaii, Honolulu, HI, USA. [20]Department of Astrophysical and Planetary Sciences, University of Colorado, Boulder, CO, USA. [21]Lunar and Planetary Laboratory, The University of Arizona, Tucson, AZ, USA. [22]Komaba Institute for Science, The University of Tokyo Komaba, Meguro, Tokyo, Japan. [23]Astrobiology Center, Osawa, Mitaka, Tokyo, Japan. [24]Department of Astronomy, California Institute of Technology, Pasadena, CA, USA. [25]Department of Physics and Astronomy, University of New Mexico, Albuquerque, NM, USA. [26]Oukaimeden Observatory, High Energy Physics and Astrophysics Laboratory, Cadi Ayyad University, Marrakech, Morocco. [27]Space Sciences, Technologies and Astrophysics Research (STAR), Institute, University of Liège, Liège, Belgium. [28]Department of Astronomy, Graduate School of Science, The University of Tokyo, Hongo, Bunkyoku, Tokyo, Japan. [29]Department of Astronomical Science, The Graduated University for Advanced Studies, Sokendai, Osawa, Mitaka, Tokyo, Japan. [30]Department of Multi-Disciplinary Sciences, Graduate School of Arts and Sciences, The University of Tokyo, Komaba, Meguro, Tokyo, Japan. [31]Department of Astrophysical Sciences, Princeton University, Princeton, NJ, USA. [32]Department of Earth, Atmospheric and Planetary Sciences, Massachusetts Institute of Technology, Cambridge, MA, USA. [33]Department of Aeronautics and Astronautics, MIT, Cambridge, MA, USA. [34]Department of Astronomy, University of California, Los Angeles, Los Angeles, CA, USA. [35]NASA Ames Research Center, Mountain View, CA, USA. [36]The SETI Institute, Mountain View, CA, USA. [37]Texas State University, Department of Physics, San Marcos, TX, USA. [38]Max-Planck Institute for Astronomy, Heidelberg, Germany. [39]Vatican Observatory Research Group, University of Arizona, Tucson, AZ, USA. [40]Graduate Institute of Astronomy, National Central University, Taoyuan, Taiwan. [41]Space Telescope Science Institute, Baltimore, MD, USA. [42]Department of Physics and Astronomy, Swarthmore College, Swarthmore, PA, USA. [43]George Mason University, Fairfax, VA, USA. [44]American Association of Variable Star Observers, Cambridge, MA, USA. [45]Tsinghua International School, Beijing, China. [46]Department of Physics and Astronomy, University of Louisville, Louisville, KY, USA. [47]National Astronomical Observatories of China, Chinese Academy of Sciences, Beijing, China. [48]SUPA Physics and Astronomy, University of St. Andrews, Fife, UK. [49]South African Astronomical Observatory, Cape Town, South Africa. [50]Google LLC, Mountain View, CA, USA. [51]NASA Goddard Space Flight Center, Greenbelt, MD, USA. [52]University of Maryland, Baltimore County, Baltimore, MD, USA. ✉e-mail: bjorn.benneke@umontreal.ca

Article

Methods

Stellar characterization

We refine the stellar radius of LP 791-18 reported in the TESS Input Catalog v.8 (refs. 4,31) using the same method as used for TRAPPIST-1 and other late-M dwarfs[32]. For that, we construct an expanded 0.3–17 μm spectral energy distribution (SED) by combining a newly obtained IRTF–SpeX Prism spectrum of LP 791-18 at 0.7–2.52 μm taken on 23 December 2020 with publicly available SDSS, PS1, 2MASS and WISE broadband measurements (Extended Data Table 3). Absolute calibration of IRTF–SpeX Prism spectrum is performed using the overlapping photometric measurements, allowing for an offset and linear trend across the spectrum. We then fill any remaining gaps in wavelength space between 0.3 and 17 μm with linear interpolation in logarithm space, and we complete the SED with a Rayleigh-Jeans tail below 0.3 μm and a Wien tail beyond 17 μm, both using the effective stellar temperature inferred from spectroscopy[4] (2,960 K). Once the SED is built, we then infer the total bolometric luminosity by scaling the SED using the measured Gaia eDR3 parallax distance of 26.65 ± 0.03 pc and integrating it over all wavelengths. We find a stellar radius of $0.182 \pm 0.007 R_{\odot}$ for LP 791-18. Our stellar radius estimate is consistent with that of ref. 4. for LP 791-18 ($0.171 \pm 0.018 R_{\odot}$) albeit with smaller radius uncertainty and inferred on the basis of the empirical reconstruction of the full SED of LP 791-18. Our inferred radius is also consistent with the overall trend in interferometric radii measurements of main-sequence late-M stars[33], in which measurements tend to indicate slightly inflated radii versus solar-metallicity models.

Transit observations

In this work, we observed a total of 72 transits of the newly discovered exo-Earth LP 791-18d and the sub-Neptune LP 791-18c using the Spitzer Space Telescope and many ground-based astronomical facilities including the Las Cumbres Observatory Global Telescope (LCOGT) network[34], MEarth[35], TRAPPIST-N/S[36], ExTrA[37], MuSCAT[38], MuSCAT2 (ref. 39). SPECULOOS[40] and the VATT and Kuiper telescopes of the EDEN network[41]. Our Spitzer observations were initially undertaken to investigate the possibility of additional terrestrial planets in the system because such planets could be dynamically stable, but could have been missed by TESS. Owing to the faintness of LP 791-18 at visible wavelengths, the TESS light curve lacked the necessary photometric precision to detect planets with radii smaller than roughly $1.2 R_{\oplus}$ at periods longer than about 1.5 days. Spitzer observed at 4.5 μm nearly continuously for 5 days from 14 to 19 October 2019, except for a 5-h break for data downlink starting 17 October at 23:30. The observations were timed to also capture two transits of planet c, with at least 2 h of baseline observations before the first transit and following the second transit. In addition to the previously known planets, the observations revealed two transits of LP 791-18d. Motivated by the detection of TTVs, we then complemented our Spitzer observations of this system with a large multi-year, multi-telescope transit campaign, consisting of 43 transit observations of the Earth-sized planet LP 791-18d and 29 transits of sub-Neptune LP 791-18c (Extended Data Tables 1 and 2 and Extended Data Fig. 1).

Initial Spitzer light-curve analysis

Our near-continuous 127-hour Spitzer light curve is divided into six light-curve segments, which we initially extract and inspect as separate light curves. For that, we first extract the photometry for each segment using a set of fixed circular apertures with sizes ranging from 1.5 to 5 pixels. For each exposure, we estimate and subtract the sky background, calculate the centroid position of the star on the detector array and then calculate the total flux within the aperture radius[42]. We find an aperture radius of 3 pixels to produce the lowest photometric scatter for all six segments. Following standard procedure, we detrend our Spitzer light-curve segments against a drift in time and intrapixel sensitivity variations using the pixel level decorrelation (PLD) approach[42,43]. Our systematics model is given by the following equation:

$$S(t_i) = \frac{\sum\limits_{k=1}^{9} w_k D_k(t_i)}{\sum\limits_{k=1}^{9} D_k(t_i)} + mt_i, \tag{1}$$

where $D_k(t_i)$ represents the raw flux in each of the nine central pixels in the target's point spread function at time t_i of the ith exposure in the photometric time series[42]. The nine PLD coefficients w_k and the linear slope m for the sensitivity drift with time are systematic parameters that are simultaneously sampled with the transit model parameters as described below.

We first perform an initial inspection of the Spitzer data by detrending each light-curve segment separately. We carefully inspect the resulting detrended photometry for decreases resembling transit-like events. In additional to the predicted transits of LP 791-18b and c, we identify two new transit events at the barycentric Julian dates (BJD) = 2458772.16 and BJD = 2458774.9 caused by planet d. We double check that these events do not align with any shift in the background flux or shift in the position of the star's centroid. The transits of planet d are marked in purple in Fig. 1 and we discuss the sensitivity of the light curve to transiting planets more quantitatively below.

Joint light-curve fitting

To determine the properties and orbits of each planet in the LP 791-18 system, we jointly analyse the TESS, Spitzer and ground-based transit photometry using ExoTEP, a modular tool designed to jointly analyse many transits from different instruments with diverse systematics models[30,42,44]. The analysis makes use of the AI-MCMC Ensemble sampler emcee package[8], combined with the batman package for efficient transit light-curve modelling[45]. We jointly fit all observed transits of each planet and derive the joint posterior distribution of the transit light-curve model parameters, the systematics model parameters for the Spitzer and ground-based light curves, and a photometric scatter value for each transit light curve. The transit light-curve model for a given planet shares the same impact parameter b and semimajor axis $a/R_{\star}$, with only the transit depth and the limb darkening coefficients assigned separately for each instrument bandpass.

For Spitzer, we simultaneously fit the PLD systematics model parameters described above, whereas the TESS and ground-based transits are detrended before fitting. For the TESS observations, we use the TESS Presearch Data Conditioning Simple Aperture Photometry[46–48] as produced by the TESS Science Processing Operations Center[49], which have been further detrended using quaternions to remove non-astrophysical systematics. To remove any remaining systematics, the TESS light curve was detrended with a Gaussian process with squared exponential kernel and a fixed length scale of 1.0 days. The LCOGT light curves are extracted using the open-source tool AstroImageJ[50], and like all ground-based light curves, are detrended against airmass. The MEarth transits, which initially showed systematics possibly caused by water column variation, were additionally detrended using a spline fit that excluded the in-transit data. The first transits of planet b and c in the Spitzer data are overlapping and, for this case, we fit the transits of planet b, planet c and the PLD systematics model simultaneously.

For limb darkening, we use the priors on the quadratic limb darkening coefficients determined for the TESS light curves of LP 791-18 (ref. 4). For the ground-based instruments we use equivalent priors determined with LDTK[51] as listed in Extended Data Table 3. For Spitzer, we choose to first fit the deep high-signal-to-noise ratio (SNR) Spitzer transits of planet c to empirically determine the 4.5 μm quadratic limb darkening coefficients for the star LP 791-18. The resulting Spitzer coefficients are then used as priors when fitting planets b and d. The photometric scatter is a free parameter for each transit, except for the TESS data, for which only one scatter parameter is shared by all transits as the overall TESS light curve has a near-constant scatter dominated across photon noise.

The Markov chain Monte Carlo (MCMC) fit for each planet is performed with four walkers per fitting parameter and run for a total of 16,000 steps, much longer than needed for formal convergence. Disregarding the initial 60% of our chains as burn-in, the resulting transit parameters and calculated properties are recorded for each planet in Extended Data Table 4. Transits from ExTrA and SPECULOOS (SSO I+z band) are not included in the joint fits, but were used in the TTV analysis. The ExTrA observations were detrended and fit using the package juliet[52] with Gaussian detrending, and with all transit parameters but the timing fixed to the results of our joint fit. The SPECULOOS and/or SSO (I+z) observations are detrended using polynomials of variable order in airmass, background and position[53].

TTV analysis

To determine the masses and orbital parameters of planets c and d, we first infer the mid-transit time for each observed transit of planet c and d by fitting each transit observation individually with ExoTEP[30,42,44]. We include Gaussian priors on all transit parameters other than the mid-transit time on the basis of the best-fit estimate from the joint fit. For Spitzer, we do a high-cadence fit directly on the basis of the tens of thousands of 2-s long exposures. All resulting light-curve fits are shown in Extended Data Fig. 1, with all the transits lined up to the mid-transit times from the best-fitting TTV model.

On the basis of the inferred mid-transit-timing estimates, we then determine the joint posterior distribution of the masses and orbital parameters of planets c and d by modelling and fitting the mid-transit times using TTVFast[7] in combination with the emcee[8] implementation of the Affine Invariant MCMC Ensemble sampler[54]. For each planet, we parameterize the pair of eccentricity e and argument of periastron ω with the pair of $e\cos\omega$ and $e\sin\omega$ at the start of the TTVFast simulation. We furthermore fit the initial transit time t_0 of the orbit at the start of the TTVFast run in place of the mean anomaly M itself because the initial transit time describes the position of the planet equivalently to M, but is much less correlated with ω, thereby facilitating the convergence substantially. Our set of $e\cos\omega$, $e\sin\omega$ and t_0 for each planet is equivalent to the set of e, ω and M. We do not include free parameters for planet b in our TTV analysis because the predicted amplitude of the TTVs for planet b are below one second, independent of the masses of planets c and d.

Using this setup, we compare two TTV analyses with different choices for the eccentricity prior. The first analysis uses a non-informative eccentricity prior on $e\cos\omega$ and $e\sin\omega$ (refs. 3,55), whereas the second analysis takes into account that tidal damping in the LP 791-18 system should have dampened the free eccentricities of the planetary orbits[56] on timescales short compared to the age of the system (Extended Data Fig. 3). This does not mean that the overall eccentricities of the planets are zero. Instead, tidal damping in the LP 791-18 system should only have dampened the free eccentricities, whereas a significant forced eccentricity on LP 791-18d can be preserved due to the mutual interaction between LP 791-18c and d (ref. 56) (Extended Data Fig. 3). We implement this tidally damped-state prior on the free eccentricities by first computing the free and forced eccentricity components for planets c and d for each proposed set of MCMC fitting parameters and then imposing Gaussian priors on the values of the free eccentricities centred at zero and with a standard deviation of 0.001. The result is a tidally damped-state prior that effectively constraints the fits to systems with near-zero free eccentricities without enforcing zero overall eccentricity at the initialization of the TTVFast simulation. The free and forced eccentricity components are calculated numerically by running rapid N-body integrations of the LP 791-18 system for each proposed set of MCMC parameters using the REBOUND library[57,58] and fitting a circle to the eccentricity vectors found by the N-body integration over time. The centre of this circle represents the free eccentricity of the planet, whereas the circle radius represents the forced eccentricity of the planet[56]. We use the WHFast integrator, 1×10^4 time steps per orbit of the closest planet, and simulate the orbits for 2 years, which is sufficient

to capture many of the 26-day super-periods of planets c and d. In addition, in all TTV analyses, we include a Gaussian prior for the stellar mass as listed in Extended Data Table 3, and we fix the inclination to the results from the joint light-curve fit and the longitude of the ascending node to $\pi/2$. We use uniform priors for the planet masses.

We find that both TTV analyses, with and without the tidally damped-state prior, provide adequate fits to all 72 transit timing measurements and consistent planet masses. A marginally better fit is obtained in the analysis without the tidally damped-state prior, which allows for non-zero free eccentricities ($\chi^2/N = 0.92$). However, given that the TTV analyses with tidally damped-state prior also adequately fits all 72 transit timing measurements ($\chi^2/N = 1.1$) and given that the tidal circularization timescale is short compared to the age of the system (Extended Data Fig. 3), we report the results from the TTV analyses with tidally damped-state prior in Extended Data Table 4. We then conservatively use only the forced eccentricity component, directly introduced by planet c, when calculating the tidal heating rate for LP 791-18d (Fig. 3). If any free eccentricity existed in the system, this would additionally increase the tidal heating rate for LP 791-18d.

Finally, we double check that the TTV solutions are not affected by any potential outliers in the mid-transit timing measurements. For that, we make eight repeats of the TTV analyses. Four repeats use all measured mid-transit times listed in Extended Data Tables 1 and 2 (A1–A4), whereas the other four repeats (B1–B4) explicitly exclude transits with relatively lower SNR or short pre- or post-transit baselines (Observations d2, d3, d9, d15, d17, d36, d38 and c21). The four separate TTV analyses for each set (A and B) are then performed using four different likelihood models. The first likelihood model assumes standard Gaussian uncertainties with the nominal error bars directly taken from Extended Data Tables 1 and 2 (Analyses A1 and B1). The second likelihood model also assumes Gaussian noise, but additionally includes an uncertainty scaling factor V_1 (analyses A2 and B2). The third likelihood model explicitly accounts for a possibly wider tail in the mid-transit timing uncertainties using a Student's t-distribution with two degrees of freedom for the observational uncertainties ($\nu = 2$)[59] (analyses A3 and B3). Finally, the fourth likelihood model uses the most general form of the Student's t-distribution simultaneously fitting both the uncertainty scaling factor $\log(V_1)$ and as well as the degrees of freedom ν (ref. 3) (analyses A4 and B4). For the last two cases, the log likelihood function of the Student's t-distribution for each data point i is given by

$$
\begin{aligned}
\log\mathcal{L}_i(\theta, \nu, V_1) = {} & \frac{\nu+1}{2}\log\left(1 + \frac{(t_{\mathrm{obs},i} - t_{\mathrm{model},i}(\theta))^2}{\nu\sigma_i V_1}\right) - \frac{1}{2}\log(\pi\nu V_1) \\
& + \log\Gamma\left(\frac{\nu+1}{2}\right) - \log\Gamma\left(\frac{\nu}{2}\right),
\end{aligned}
\tag{2}
$$

where $\Gamma(x)$ is the Gamma function, $t_{\mathrm{obs},i}$ are the observed mid-transit times and $t_{\mathrm{model},i}(\theta)$ are the mid-transit times predicted by the model for a given set of planet and orbital parameters θ. The total log likelihood is obtained by summing all the log likelihood values for the individual data points. We perform repeated emcee runs from widely different starting conditions, and we use up to 880 walkers (80 walkers per fitting parameter) and 15,000 steps, many times beyond the formal convergence criterion. We obtain consistent results for all eight independent analyses (A1–B4). In particular, the inferred planet masses and orbital eccentricities of planets c and d agree within their uncertainties.

Note that during our entire work, we exclude one MEarth-N transit of planet d taken 8 February 2020 (Exoplanet Follow-up Observing Program (ExoFOP) tag ID 16501) as this transit is incomplete, an LCOGT observation taken on 17 March 2020 (tag ID 18144) affected by clouds passing during pretransit, as well as one SPECULOOS South transit of planet d taken on 4 March 2020, which was affected by systematics in the light curve and disagreed with the four transit times obtained with MuSCAT2, MEarth-S, TRAPPIST-N and LCOGT-CTIO observation during the same night.

Article

Tidal damping analysis

To investigate the tidal damping of free eccentricities in the LP 791-18 system, we perform N-body integrations using the symplectic Wisdom–Holman integrator WHFast with tidal heating implemented in the REBOUNDx libraries[57,58,60]. We use the masses of planet c and d as inferred in the TTV analysis and assume an Earth-like iron-rock composition for planet b ($M_b = 1.8 \, M_\oplus$). We then initiate the orbits of the three planets with the three semimajor axes inferred from the planets' measured orbital periods (Extended Data Table 4) and deliberately impose substantial initial free eccentricities between 0.02 and 0.05. The N-body integration then models the evolution of the three orbits due to tidal damping and the planets' mutual gravitational interaction. We find that the free eccentricities are rapidly damped over timescales short compared to the age of the system (Extended Data Fig. 3). This is true even when the tidal quality factors is significantly increased above the generally assumed values of $Q_p = 10$–100 for terrestrial planets[61]. We find that the dynamical evolution remains rapid and qualitatively similar to Extended Data Fig. 3 even for tidal quality factors of $Q_p = 1,000$ for LP 791-18b and LP 791-18d or a Neptune-like tidal quality factor of $Q_p = 2 \times 10^5$ for the sub-Neptune LP 791-18c. We note, however, that despite the tidal damping, a significant non-zero forced eccentricity circulating around 0.0015 is preserved for LP 791-18d.

System stability analysis

We perform N-body integrations of the LP 791-18 system using the REBOUND library[57,58], choosing the symplectic Wisdom–Holman integrator WHFast. As a conservative approach, we choose the highest allowed masses and eccentricities within error bars for planets c and d. The eccentricity of planet b is not observationally constrained; however, assuming an effective rigidity $\tilde{\mu} = (10^4 \mathrm{km}/R_p)^2$, a tidal quality factor $Q_p = 100$, and a planet mass of $M_b = 1.8 \, M_\oplus$ for a Earth-like iron-rock composition, we argue that the tidal circularization timescale of planet b[62]

$$\tau_e = \frac{4}{63} \frac{\tilde{\mu} Q_p}{2\pi} \frac{M_p}{M_*} \left(\frac{a}{R_p} \right)^5 P \tag{3}$$

is only τ_e of roughly 4.2×10^4 years and much shorter than the age of the system. For the N-body integrations, we therefore initialize planet b's orbit with an eccentricity near zero (0.01) and take the semimajor axis a and R_p of planet b from Extended Data Table 4. We furthermore assume zero inclination for all objects for the N-body integrations. We integrate the system for 10^9 orbits of planet c, with a time step of 0.1 days. This timescale is long enough to allow for secularly driven and chaotic diffusive instabilities to manifest if present. We run ten simulations with random initial anomalies and arguments of periapsis, and find them all to be stable with no extreme eccentricity excitation for any object. An example simulation is shown in Extended Data Fig. 4a,b.

Stability of LP 791-18 with hypothetical additional planets

To assess whether the system can dynamically accommodate a fourth unseen planet, we run a suite of N-body integrations with one additional hypothetical planet introduced on a circular orbit in each simulation. Across the simulations, the semimajor axis of the hypothetical planet ranges between 0.015 and 0.045 astronomical units (AU), that is, we consider a wide range of orbits from interior to LP 791-18d to orbits exterior to the outermost planet LP 791-18c. Representative scenarios with a hypothetical $1 \, M_\oplus$ planet at different locations in the system are shown in Extended Data Fig. 4c–h. The system stability simulations are performed as before, but using the higher-order IAS15 integrator available in the REBOUND library. We find that the system can accommodate a $1 \, M_\oplus$ planet with semimajor axes near 0.015 AU (between planets b and d) without triggering dynamical instability (Extended Data Fig. 4c,d). Similarly, a planet in an orbit sufficiently outside planet c can be stable (Extended Data Fig. 4e,f). On the other hand, any planet orbiting between planet d and c or any planet orbiting too closely exterior of planet c (for example, at 0.035 AU) will quickly make the system unstable, with either planet d or the fictional planet being ejected (Extended Data Fig. 4g,h). These findings are equivalent for hypothetical planets with substantially lower mass ($0.1 \, M_\oplus$) or higher mass ($2 \, M_\oplus$).

Interior modelling and susceptibility to mass loss

We interpolate over a grid of interior models with Earth-like core compositions and solar-composition hydrogen envelopes[9] to estimate the maximum amount of hydrogen that could be present on LP 791-18d today[63]. We take into account the present-day insolation of LP 791-18d and conservatively assume a stellar age of 10 Gyr because any gas envelopes, if present, would shrink as the planet cools with age. We find that even the lowest hydrogen-mass fraction in the grid (0.01%) corresponds to a radius of $1.23 \, R_\oplus$, whereas LP 791-18d has a radius of only $1.03 \pm 0.04 \, R_\oplus$ (Extended Data Fig. 5). We therefore take 0.01% as a conservative upper limit on the amount of hydrogen that can at present be accommodated by the measured planet parameters. The long-term stability of such a hypothetical low-mass hydrogen-dominated envelope of less than $0.0001 \, M_\oplus$ is, however, put into question from basic atmospheric escape considerations. We estimate hydrogen-mass-loss rates for hydrostatic Jeans escape as well as hydrodynamic energy-limited escape, and find in both cases that even the highly conservative 0.01% hydrogen envelope would be quickly lost on timescales of 10–500 Myr.

For Jeans escape, we use equation 1 from ref. 64. to estimate the escape flux for various particle number densities and temperatures n_{exo} and T_{exo} at the exobase. We find envelope loss timescales $\tau_{esc} = M_{env}/\dot{M}_{env}$ of the order of 10–100 Myr for n_{exo} similar Earth or Jupiter[65,66], with the exact value depending on the assumed exobase altitude and temperature at the exobase[67]. If the upper atmosphere were puffed up by absorption of high-energy stellar radiation[63], the high altitude of the exobase and larger kinetic energy of atmospheric particles would further loosen the particles' gravitational binding and make the atmosphere even more susceptible to escape. Equivalently, we estimate an escape flux for hydrodynamic energy-limited escape:

$$\dot{M} = \eta \frac{\pi R_p R_{eff}^2 L_{HE}}{4\pi a^2 G M_p} f(A) \tag{4}$$

where η is the mass-loss efficiency ($\eta < 1$ to accounts for energy losses), R_p is the planet radius, R_{eff} is the effective radius of the photosphere at extreme ultraviolet (XUV) wavelengths that can reach several times R_p, L_{HE} is the star's high-energy luminosity, a and M_p are the semimajor axis and mass of the planet, and the factor $f(A)$ (roughly 1.04 to 1.07) accounts for the enhanced atmospheric mass loss in the presence of stellar flares[14,68]. Our prescription for the high-energy luminosity L_{HE} is the same as in previous work[69], with a constant luminosity for the first 100 Myr and a logarithmic decay over the rest of the star's lifetime[14,70–73]. We use $\eta = 10\%$, appropriate for super-Earths and sub-Neptunes[74]. We derive atmosphere loss timescales for $R_{eff} = 1$ to $2R_p$ of 30–200 Myr for a 1 Gyr old star or 100–600 Myr for a 10 Gyr old star for the conservatively assumed 0.01% hydrogen envelope.

For the sub-Neptune LP 791-18c, we perform a Bayesian analysis to constrain its composition using the open-source smint[69] tool and the model grid from ref. 9. We find a hydrogen-mass fraction of $2.0^{+0.6}_{-0.5}\%$ to match observed radius for a core with Earth-like composition (Extended Data Fig. 5). Such a massive hydrogen envelope could be maintained over Gyr timescales on LP 791-18c.

Testing consistency with models of photoevaporation and core-powered mass loss

We use the ratio of the mass-loss timescales of LP 791-18c and LP 791-18d to assess whether the planet pair is consistent with the predictions from both the photoevaporation[14,75] and core-powered mass-loss models[15,76] as possible explanations for the origin of the radius valley[11]. In both

models, the initial condition is assumed to be a population of planets with H or He envelopes, out of which the planets that eventually end up below the radius valley lose their envelopes by means of thermal escape either driven by XUV heating from the host star (photoevaporation) or driven by the planetary core's own cooling luminosity (core-powered mass loss). Systems with several transiting planets are well-suited for testing these models by means of mass-loss timescales arguments because the poorly constrained XUV and bolometric luminosity histories of the host star cancel out when computing the ratio of the mass-loss timescales of two planets orbiting the same star. LP 791-18c and d is a special pair because it is the first time that the photoevaporation and core-powered mass-loss models are tested for planets orbiting a late-M dwarf, and in addition in orbits with low equilibrium temperatures. We thus compute the ratios of the mass-loss timescales of LP 791-18c and d as

$$\frac{t_{\text{loss,c}}}{t_{\text{loss,d}}} = \frac{(M_c/M_\oplus)^{0.64}}{M_d/M_\oplus}\left(\frac{a_c}{a_d}\right)^{2/3}(R_d/R_\oplus)^{4/3} \tag{5}$$

for the photoevaporation model[17,75] and as

$$\frac{t_{\text{loss,c}}}{t_{\text{loss,d}}} = \frac{M_c}{M_d}\left(\frac{T_{\text{eq,c}}}{T_{\text{eq,d}}}\right)^{-3/2}\exp\left[c'\left(\frac{M_c}{T_{\text{eq,c}}R_c} - \frac{M_d}{T_{\text{eq,d}}R_d}\right)\right] \tag{6}$$

for the core-powered mass-loss model[15,17,76]. Here, M is the planet mass, a is the orbital semimajor axis, R is the planet radius and T_{eq} is the equilibrium temperature, with the indices indicating planet c or d. The constant c' is approximately equal to $10^4 R_\oplus K M_\oplus^{-1}$. Several assumptions were made in the derivation of equation (5) including that the mass-loss efficiency under the photoevaporation model is antiproportional to the square of the escape velocity[14], that the planet cores have Earth-like compositions and that the planet masses are dominated by the core masses. In addition, for the core-powered mass-loss model, equation (6) assumes that most of the atmospheric gas lies within its convective zone and that the radius at the radiative–convective boundary is equal to the measured planet radius[17]. Using equations (5) and (6), we plot the posterior distributions of the mass-loss timescale ratios for LP 791-18c and d under the models of photoevaporation and core-powered mass loss in Extended Data Fig. 6. We find that the pair of the sub-Neptune LP 791-18c and the Earth-sized planet LP 791-18d is consistent with both the models of photoevaporation and core-powered mass loss for all planet masses, radii and semimajor axis consistent with observational uncertainties.

Tidal synchronization

We investigate whether LP 791-18d is tidally locked by computing its tidal synchronization timescale τ_{syn} (ref. 77) and comparing it to the lower limit on the LP 791-18 system's age of 500 Myr (Extended Data Table 3). Owing to LP 791-18d's small semimajor axis and short orbital period, we find that the tidal synchronization timescale is much shorter than the system's age for all plausible values of the tidal quality factor Q. For $Q_p = 10$–100 characteristic of rocky planets[61], we obtain τ_{syn} equal to only 3–30 years corresponding to a few thousand orbital periods. Even for a $Q_p = 10^{6.5}$ typical of gaseous planets[78], we would obtain 1 Myr for the tidal synchronization timescale, which remains orders of magnitude shorter than the lower inferred limit on the system's age. Finally, the possibility of capture into a higher spin-orbit resonance is also extremely unlikely due to the strong dissipative tidal torque exerted on the planet for an orbit as compact as that of LP 791-18d (ref. 79). Similarly, thermal tides in the atmosphere are unable to significantly affect the spin of a planet this close to a low-mass star[80]. We conclude that the planet is extremely likely to be tidally locked in a spin-orbit synchronous resonance.

Tidal heating model

We use the tidal heating model previously applied to the interior of Io[81–84] and the TRAPPIST-1 planets[85], as implemented within the open-source tool melt. Assuming that the planet is in synchronous rotation, we calculate its tidal energy dissipation as:

$$\dot{E}_{\text{tidal}} = -\frac{21}{2}\text{Im}(k_2)\frac{R^5\omega^5 e^2}{G}, \tag{7}$$

where R and e are the planet's radius and orbital eccentricity, $\text{Im}(k_2)$ is the imaginary part of the planet's Love number, G is the gravitational constant and ω is equal to $2\pi/P$ with P being the orbital period[86]. Instead of using a fixed tidal quality factor Q to assess the rate of energy dissipation per tidal cycle, we adopt the Maxwell model of viscoelastic rheology to take into account the feedback between the thermal state of the planet's interior and its response to tidal forcing. In the Maxwell model, $\text{Im}(k_2)$ is evaluated as:

$$\text{Im}(k_2) = -\frac{57\eta\omega}{4\bar{\rho}gR\left[1 + \left(1 + \frac{19\mu}{2\bar{\rho}gR}\right)^2\frac{\eta^2\omega^2}{\mu^2}\right]} \tag{8}$$

where η is the viscosity of the material, μ is the shear modulus, $\bar{\rho}$ is the average density of the planet and g the surface gravity of the planet[81–85]. We then obtain the mantle equilibrium temperature T_{mantle} as the temperature for which the globally averaged tidal heat flux $F_{\text{tidal}} = \dot{E}_{\text{tidal}}/4\pi R^2$ is in balance with the rate of radial energy transport towards the surface by means of convection F_{conv} (refs. 85,87,88), that is, satisfying:

$$\frac{\dot{E}_{\text{tidal}}(T_{\text{mantle}})}{4\pi R^2} = 0.53\left(\frac{Q^\star}{R_G T_{\text{mantle}}^2}\right)^{-4/3}\left(\frac{\rho g\alpha k_{\text{therm}}^3}{\kappa_{\text{therm}}\eta(T_{\text{mantle}})}\right)^{1/3}. \tag{9}$$

Here, R_G is the universal gas constant, and the properties of rock are used for the activation energy $Q^\star = 333$ kJ mol^{-1}, the coefficient of thermal expansion $\alpha = 3\times10^{-5}$ K^{-1} and the thermal diffusivity $\kappa_{\text{therm}} = k_{\text{therm}}/(\rho C_p)$ with $k_{\text{therm}} = 3.2$ W m^{-1} K^{-1} and $C_p = 1,200$ J kg^{-1}. For the density we use $\rho = 5,000$ kg m^{-3}, appropriate for a pure rock composition[87]. $\dot{E}_{\text{tidal}}$ depends on T_{mantle} in equation (9) by means of the temperature dependence of the shear modulus μ and the viscosity η. At temperatures below the solidus of rock ($T_s = 1,600$ K), we use $\mu = 50$ GPa and $\eta(T) = \eta_0\exp(Q^\star/(R_G T))$ with $\eta_0 = 2.13\times10^6$ Pas (refs. 81,83). Between the solidus temperature and the 'breakdown point' ($T_b = 1,800$ K), which marks the transition to a regime in which the shear stiffness becomes negligible[89], we use the shear modulus $\mu(T) = 10^{\frac{\mu_1}{T}+\mu_2}$ where $\mu_1 = 8.2\times10^4$ K and $\mu_2 = -40.6$. The viscosity in this regime is described as $\eta(T) = \eta_0\exp(Q^\star/(R_G T))\exp(-Bf)$, where the melt fraction coefficient B describes the dependency of the rock viscosity on the melt fraction f and experimentally constrained to be between 10 and 40 (ref. 82). The melt fraction f, in turn, increases linearly from 0 to 0.5 between T_s and T_b (refs. 81,82).

For LP 791-18d, specifically, we compute the equilibrium mantle temperature and the corresponding tidal heat flux using the median parameters in Extended Data Table 4. We explore the full range of experimentally determined values for the melt fraction coefficient B of rock between 10 and 40 (ref. 82). We find that, as LP 791-18d cooled down, equilibrium occurred for $T > T_s$ for all values of B, which is a stable equilibrium[82,84]. The corresponding tidal flux at the planet's surface is 0.2–0.9 W m^{-2} depending on the exact value of melt fraction coefficient (Fig. 3). Surface volcanic eruptions are an expected consequence of the tidal heating if the rocky mantle reaches up to the planetary surface. The tidal heating thus probably results in the presence of permanent molten magma over the lifetime of the system, with volcanic activity potentially similar to that on Jupiter's volcanically active moon Io[5,6].

Spitzer sensitivity tests

To determine whether additional transiting planet could exist without being detected in the Spitzer light curve, we perform a suite of

Article

injection-and-recovery tests. First, we evaluate the sensitivity of the Spitzer observations to small planet between planets b and d. We generate 180,000 transit signatures for planets with radii randomly distributed between 0.5 and 1.0 Earth radii, transit impact parameters randomly distributed between 0 and 0.8, and orbital periods randomly sampled from a log-uniform distribution between 0.5 and 2.4 days. We then inject these simulated transit signatures into the Spitzer light curve at four random phases, one at a time, and measure the χ^2 improvement of the transit model versus a straight line on the injected light curve. In total, this results in 720,000 injections and χ^2 values. We then randomly selected 6,000 of these injections and run a transit recovery search on them. We model the recovery rate as a function of the χ^2 improvement of the injected signals and use this to calculate a theoretical recovery rate for each signal. These rates are then binned by period and radius to determine which sizes of planets could be missed in the Spitzer data at different orbital periods. We conclude that any transiting planets between planets b and d with radii larger than roughly $0.8\,R_\oplus$ should have been detected by the Spitzer observations with a probability greater than 90%.

In a separate analysis, we furthermore investigate the sensitivity of the Spitzer photometry to single-transit events. We find that any single transit of a planet larger than $1.2\,R_\oplus$ should have been detected at a probability greater than 95%. As we detect no additional single-transit event in the data, we conclude that such transiting planets in longer periods either do not exist or did not transit during the 127 h (5.3 days) we observed. Assuming random orbital phase, our detection fraction for planets larger than $1.2\,R_\oplus$ outside the orbit of planet c is therefore simply the amount of time observed (5.3 days) divided by the period of the hypothetical planet.

Discussion of LP 791-18d's climate state
3D global climate models predict the possibility of two stable climate regimes for Earth-sized planets such as LP 791-18d near the inner edge of the habitable zone, resulting from a competition between the greenhouse effect and the condensation of the greenhouse gases H_2O and CO_2 on the cold night side[22]. LP 791-18 may have entered a Venus-like runaway greenhouse state[20,21]. In this regime, the tidally locked planet could initially have formed a thick layer of highly reflective clouds at the permanent substellar point[20,90], which would have lowered the globally averaged equilibrium temperature to near 300 K for a Venus-like albedo. However, in this regime, large amounts of water could still have been lost to space over the lifetime of the system, plausibly leaving the planet dry. Alternatively, if the initial heat redistribution to the night side was weak, LP 791-18d's atmosphere could have entered a 'collapsed' regime, with water being captured in permanent cold traps on the night side or near the poles[22,23]. As more of the greenhouse gases condensed, the atmosphere would have cooled down further, thereby accelerating the condensation. The result could be a thick ice cap on LP 791-18d's night side. Temperatures would probably be too low for liquid surface water on the night side; however, the considerable geothermal flux (Fig. 3) combined with high pressures reached at the bottom of the ice caps could result in subsurface liquid water[22]. A sufficiently thick ice cap on the night side could then plausibly also trigger gravity-driven glacial ice flows transporting ice towards the warmer regions near the terminator where it could melt to form liquid surface water[22].

Prospects for future atmospheric characterization
So far, the planets in the TRAPPIST-1 system are the only temperate (lower than 400 K) Earth-sized planets approved for substantial James Webb Space Telescope (JWST) observations for spectroscopic follow-up studies. However, there remains a possibility that all the TRAPPIST-1 planets have a common formation and evolution history[3], which may have left the system volatile-poor and the planets bare without atmospheres. LP 791-18d presents a powerful opportunity to spectroscopically study a temperate Earth-sized planet outside the TRAPPIST-1 system,

in particular in a system where at least one planet (LP 791-18c) accreted and retained a substantial amount of gas and volatiles. From an observational perspective, LP 791-18's small stellar radius ($0.182 \pm 0.007\,R_\odot$) and extremely low stellar luminosity ($0.00230 \pm 0.00001\,L_\odot$) make LP 791-18d an exceptional M star opportunity, especially because the stellar radius shrinks rapidly beyond spectral type M4-5[1]. The observable transit depth contrast between inside and outside atmospheric absorption bands in LP 791-18d's transmission spectrum should be as high as 30–100 ppm even for compact high-mean molecular-weight terrestrial atmospheres, such as CO_2-dominated, N_2-dominated or H_2O atmospheres, despite the planet's small size and low temperature (Fig. 4). Such transit depth contrasts across the spectrum are well above the expected systematic noise floor of JWST instruments[27] and LP 791-18d's high Transit Spectroscopy Metric[26] combined with frequently occurring transit events allows for efficient exploration of LP 791-18d's atmosphere, its climate state and possibly its planetary geochemistry.

Data availability
The Spitzer data used in this study are publicly available at the Spitzer Heritage Archive, https://sha.ipac.caltech.edu/applications/Spitzer/SHA. The ground-based telescope observations are uploaded to ExoFOP and are publicly available. Source data are provided with this paper.

Code availability
We fit the light-curve data using the open-source tools emcee and batman, available at https://github.com/dfm/emcee and https://github.com/lkreidberg/batman. The TTVs are modelled using the open-source tool TTVFast, available at https://github.com/kdeck/TTVFast, and are also fit using emcee. We obtain the constraints on planet compositions using the open-source tool smint, available at https://github.com/cpiaulet/smint. The tidal heating energy balance calculations are performed with the open-source tool melt, available at https://github.com/cpiaulet/melt.

31. Stassun, K. G. et al. The revised TESS input catalog and candidate target list. *Astron. J.* **158**, 138 (2019).
32. Filippazzo, J. C. et al. Fundamental parameters and spectral energy distributions of young and field age objects with masses spanning the stellar to planetary regime. *Astrophys. J.* **810**, 158 (2015).
33. Demory, B.-O. et al. Mass-radius relation of low and very low-mass stars revisited with the VLTI. *Astron. Astrophys.* **505**, 205–215 (2009).
34. Brown, T. M. et al. Las Cumbres observatory global telescope network. *Publ. Astron. Soc. Pac.* **125**, 1031 (2013).
35. Nutzman, P. & Charbonneau, D. Design considerations for a ground-based transit search for habitable planets orbiting m dwarfs. *Publ. Astron. Soc. Pac.* **120**, 317–327 (2008).
36. Gillon, M. et al. The TRAPPIST survey of southern transiting planets—I. Thirty eclipses of the ultra-short period planet WASP-43 b. *Astron. Astrophys.* **542**, A4 (2012).
37. Bonfils, X. et al. in *Techniques and Instrumentation for Detection of Exoplanets VII* Vol. 9605 96051L (International Society for Optics; Photonics, 2015).
38. Narita, N. et al. MuSCAT: a multicolor simultaneous camera for studying atmospheres of transiting exoplanets. *J. Astron. Telesc. Instrum. Syst.* **1**, 045001 (2015).
39. Narita, N. et al. MuSCAT2: four-color simultaneous camera for the 1.52-m Telescopio Carlos Sánchez. *J. Astron. Telesc. Instrum. Syst.* **5**, 015001 (2018).
40. Murray, C. A. et al. Photometry and performance of SPECULOOS-South. *Mon. Not. R. Astron. Soc.* **495**, 2446–2457 (2020).
41. Gibbs, A. et al. EDEN: sensitivity analysis and transiting planet detection limits for nearby late red dwarfs. *Astrophys. J.* **159**, 169 (2020).
42. Benneke, B. et al. Spitzer observations confirm and rescue the habitable-zone super-earth K2-18b for future characterization. *Astrophys. J.* **834**, 187 (2017).
43. Deming, D. et al. Spitzer secondary eclipses of the dense, modestly-irradiated, giant exoplanet HAT-P-20b using pixel-level decorrelation. *Astrophys. J.* **805**, 132 (2015).
44. Benneke, B. et al. A sub-Neptune exoplanet with a low-metallicity methane-depleted atmosphere and Mie-scattering clouds. *Nat. Astron.* **3**, 813–821 (2019).
45. Kreidberg, L. Batman: basic transit model calculation in Python. *Publ. Astron. Soc. Pac.* **127**, 1161 (2015).
46. Stumpe, M. C. et al. Kepler presearch data conditioning I—architecture and algorithms for error correction in Kepler light curves. *Publ. Astron. Soc. Pac.* **124**, 985 (2012).
47. Smith, J. C. et al. Kepler presearch data conditioning II—a Bayesian approach to systematic error correction. *Publ. Astron. Soc. Pac.* **124**, 1000 (2012).
48. Stumpe, M. C. et al. Multiscale systematic error correction via wavelet-based bandsplitting in Kepler data. *Publ. Astron. Soc. Pac.* **126**, 100–114 (2014).
49. Jenkins, J. M. et al. in *Software and Cyberinfrastructure for Astronomy IV* Vol. 9913 (eds Chiozzi, G. & Guzman, J. C.) 1232–1251 (International Society for Optics; Photonics; SPIE, 2016).

50. Collins, K. A., Kielkopf, J. F., Stassun, K. G. & Hessman, F. V. ASTROIMAGEJ: image processing and photometric extraction for ultra-precise astronomical light curves. *Astron. J.* **153**, 77 (2017).

51. Parviainen, H. & Aigrain, S. Ldtk: limb darkening toolkit. *Mon. Not. R. Astron. Soc.* **453**, 3821–3826 (2015).

52. Espinoza, N., Kossakowski, D. & Brahm, R. Juliet: a versatile modelling tool for transiting and non-transiting exoplanetary systems. *Mon. Not. R. Astron. Soc.* **490**, 2262–2283 (2019).

53. Gillon, M. et al. The TRAPPIST survey of southern transiting planets. I. Thirty eclipses of the ultra-short period planet WASP-43 b. *Astron. Astrophys.* **542**, A4 (2012).

54. Goodman, J. & Weare, J. Ensemble samplers with affine invariance. *Commun. Appl. Math. Comput. Sci.* **5**, 65–80 (2010).

55. Eastman, J., Gaudi, B. S. & Agol, E. EXOFAST: a fast exoplanetary fitting suite in IDL. *Publ. Astron. Soc. Pac.* **125**, 83–112 (2013).

56. Lithwick, Y., Xie, J. & Wu, Y. Extracting planet mass and eccentricity from TTV data. *Astrophys. J.* **761**, 122 (2012).

57. Rein, H. & Liu, S.-F. REBOUND: an open-source multi-purpose N-body code for collisional dynamics. *Astron. Astrophys.* **537**, A128 (2012).

58. Rein, H. & Tamayo, D. WHFAST: a fast and unbiased implementation of a symplectic Wisdom-Holman integrator for long-term gravitational simulations. *Mon. Not. R. Astron. Soc.* **452**, 376–388 (2015).

59. Jontof-Hutter, D. et al. Secure mass measurements from transit timing: 10 Kepler exoplanets between 3 and 8 $M_{\oplus}$ with diverse densities and incident fluxes. *Astrophys. J.* **820**, 39 (2016).

60. Tamayo, D., Rein, H., Shi, P. & Hernandez, D. M. REBOUNDx: a library for adding conservative and dissipative forces to otherwise symplectic N-body integrations. *Mon. Not. R. Astron. Soc.* **491**, 2885–2901 (2020).

61. Clausen, N. & Tilgner, A. Dissipation in rocky planets for strong tidal forcing. *Astron. Astrophys.* **584**, A60 (2015).

62. Murray, C. D. & Dermott, S. F. *Solar System Dynamics* (Cambridge Univ. Press, 2000).

63. Piaulet, C. et al. WASP-107b's density is even lower: a case study for the physics of planetary gas envelope accretion and orbital migration. *Astron. J* **161**, 70 (2021).

64. Tian, F. Atmospheric escape from solar system terrestrial planets and exoplanets. *Ann. Rev. Earth Planetary Sci.* **43**, 459–476 (2015).

65. Liang, M.-C., Parkinson, C. D., Lee, A. Y.-T., Yung, Y. L. & Seager, S. Source of atomic hydrogen in the atmosphere of HD 209458b. *Astrophys. J. Lett.* **596**, L247–L250 (2003).

66. Lecavelier des Etangs, A., Vidal-Madjar, A., McConnell, J. C. & Hébrard, G. Atmospheric escape from hot Jupiters. *Astron. Astrophys.* **418**, L1–L4 (2004).

67. Tian, F., Toon, O. B., Pavlov, A. A. & De Sterck, H. Transonic hydrodynamic escape of hydrogen from extrasolar planetary atmospheres. *Astrophys. J.* **621**, 1049–1060 (2005).

68. Feinstein, A. D. et al. Flare statistics for young stars from a convolutional neural network analysis of TESS data. *Astron. J* **160**, 219 (2020).

69. Piaulet, C. et al. Evidence for the volatile-rich composition of a 1.5-Earth-radius planet. *Nat. Astron.* https://doi.org/10.1038/s41550-022-01835-4 (2022).

70. Ribas, I., Guinan, E. F., Güdel, M. & Audard, M. Evolution of the solar activity over time and effects on planetary atmospheres. I. High-energy irradiances (1-1700å). *Astrophys. J.* **622**, 680–694 (2005).

71. Jackson, A. P., Davis, T. A. & Wheatley, P. J. The coronal X-ray-age relation and its implications for the evaporation of exoplanets. *Mon. Not. R. Astron. Soc.* **422**, 2024–2043 (2012).

72. Tu, L., Johnstone, C. P., Güdel, M. & Lammer, H. The extreme ultraviolet and X-ray Sun in time: high-energy evolutionary tracks of a solar-like star. *Astron. Astrophys.* **577**, L3 (2015).

73. Güdel, M., Guinan, E. F. & Skinner, S. L. The X-ray sun in time: a study of the long-term evolution of coronae of solar-type stars. *Astrophys. J.* **483**, 947–960 (1997).

74. Owen, J. E. & Jackson, A. P. Planetary evaporation by UV & X-ray radiation: basic hydrodynamics. *Mon. Not. R. Astron. Soc.* **425**, 2931–2947 (2012).

75. Owen, J. E. & Campos Estrada, B. Testing exoplanet evaporation with multitransiting systems. *Mon. Not. R. Astron. Soc.* **491**, 5287–5297 (2020).

76. Ginzburg, S., Schlichting, H. E. & Sari, R. Core-powered mass-loss and the radius distribution of small exoplanets. *Mon. Not. R. Astron. Soc.* **476**, 759–765 (2018).

77. Piro, A. L. Exoplanets torqued by the combined tides of a moon and parent star. *Astron. J* **156**, 54 (2018).

78. Piro, A. L. & Vissapragada, S. Exploring whether super-puffs can be explained as ringed exoplanets. *Astron. J* **159**, 131 (2020).

79. Ribas, I. et al. The habitability of Proxima Centauri b—I. Irradiation, rotation and volatile inventory from formation to the present. *Astron. Astrophys.* **596**, A111 (2016).

80. Leconte, J., Wu, H., Menou, K. & Murray, N. Asynchronous rotation of Earth-mass planets in the habitable zone of lower-mass stars. *Science* **347**, 632–635 (2015).

81. Fischer, H.-J. & Spohn, T. Thermal-orbital histories of viscoelastic models of Io (J1). *Icarus* **83**, 39–65 (1990).

82. Moore, W. B. Tidal heating and convection in Io. *J. Geophys. Res.* **108**, 5096 (2003).

83. Henning, W. G., O'Connell, R. J. & Sasselov, D. D. Tidally heated terrestrial exoplanets: viscoelastic response models. *Astrophys. J.* **707**, 1000–1015 (2009).

84. Dobos, V. & Turner, E. L. Viscoelastic models of tidally heated exomoons. *Astrophys. J.* **804**, 41 (2015).

85. Barr, A. C., Dobos, V. & Kiss, L. L. Interior structures and tidal heating in the TRAPPIST-1 planets. *Astron. Astrophys.* **613**, A37 (2018).

86. Segatz, M., Spohn, T., Ross, M. N. & Schubert, G. Tidal dissipation, surface heat flow, and figure of viscoelastic models of Io. *Icarus* **75**, 187–206 (1988).

87. Solomatov, V. S. & Moresi, L.-N. Scaling of time-dependent stagnant lid convection: application to small-scale convection on Earth and other terrestrial planets. *J. Geophys. Res.* **105**, 21795–21818 (2000).

88. Barr, A. C. Mobile lid convection beneath Enceladus' south polar terrain. *J. Geophys. Res.* **113**, E07009 (2008).

89. Renner, J., Evans, B. & Hirth, G. On the rheologically critical melt fraction. *Earth Planet. Sci. Lett.* **181**, 585–594 (2000).

90. Yang, J., Liu, Y., Hu, Y. & Abbot, D. S. Water trapping on tidally locked terrestrial planets requires special conditions. *Astrophys. J.* **796**, L22 (2014).

91. Zeng, L., Sasselov, D. D. & Jacobsen, S. B. Mass–radius relation for rocky planets based on PREM. *Astrophys. J.* **819**, 127 (2016).

Extended Data Fig. 1 | All 72 transit observations of LP 791-18c (left) and LP 791-18d (right) lined up to their fitted mid-transit times. Circles indicate the detrended normalized flux measurements from TESS (black), Spitzer (red), LCOGT (green), EDEN (brown), MuSCAT/MuSCAT2 (dark blue), TRAPPIST telescope (purple), MEarth (yellow), ExTrA (pink), and SPECULOOS (grey), compared to the best-fitting transit models based on the transit times from the TTV analysis (solid black curve). Vertical lines indicate the 68% uncertainties. Multiple transits from a given telescope or telescope network are directly overplotted, while observations from the different telescopes are vertical offset and in different colors for clarity (Extended Data Tables 1–2).
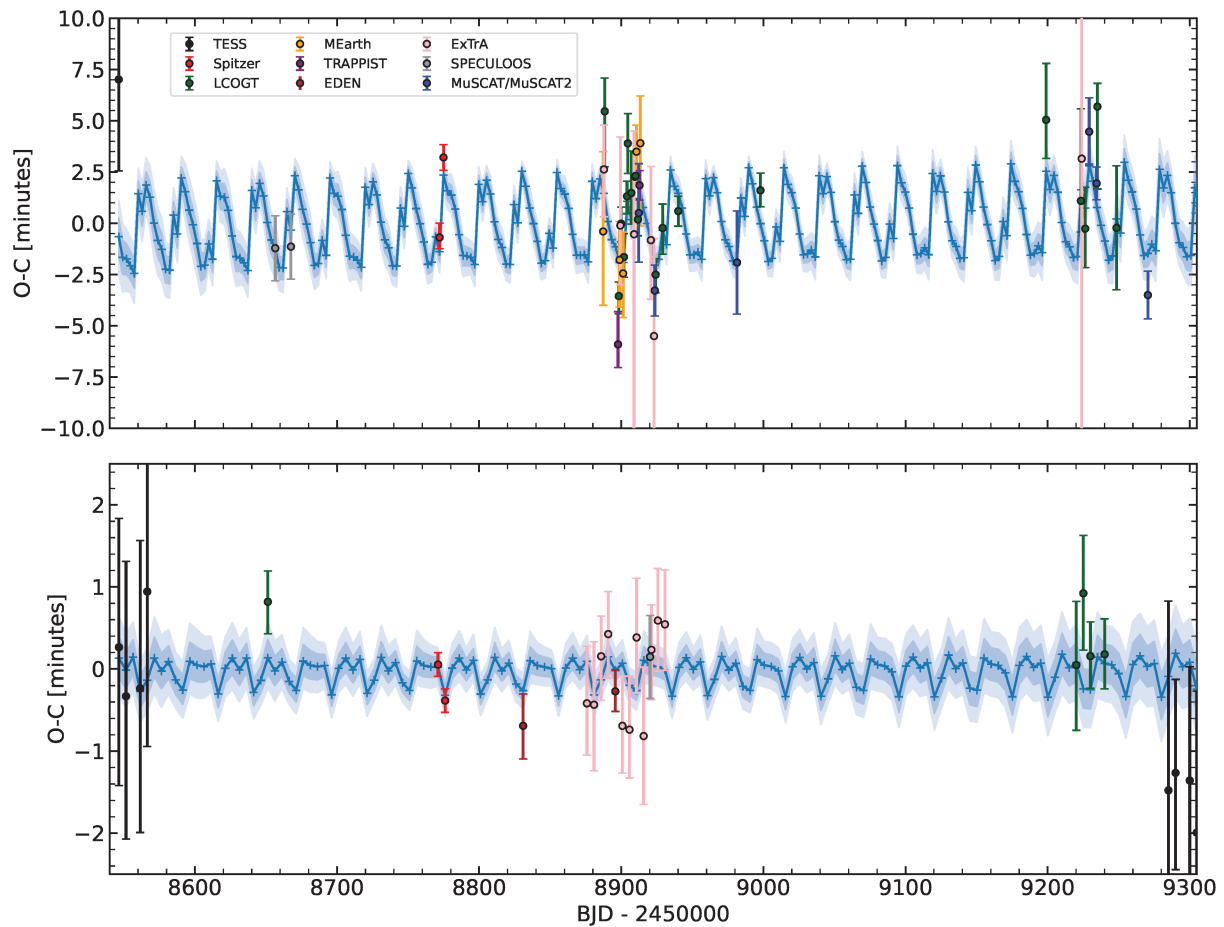
Extended Data Fig. 2 | Transit timing variations of the Earth-sized planet LP 791-18 (top panel) and the sub-Neptune LP 791-18c (bottom panel). Colored data points indicate the 72 transit timing measurements obtained with TESS (black), Spitzer (red), LCOGT (green), MEarth (yellow), TRAPPIST telescope (purple), EDEN (brown), ExTrA (pink), SPECULOOS (grey), MuSCAT/MuSCAT2 (dark blue), compared to the best-fitting TTVFast model (blue curve). The vertical axis represents the deviation from the best fitting linear ephemeris and the horizontal axis the Barycentric Julian Date (BJD) of the observation. Dark and light shaded regions illustrate the posterior population of models in the MCMC fit corresponding to 68% and 95% confidence, respectively.
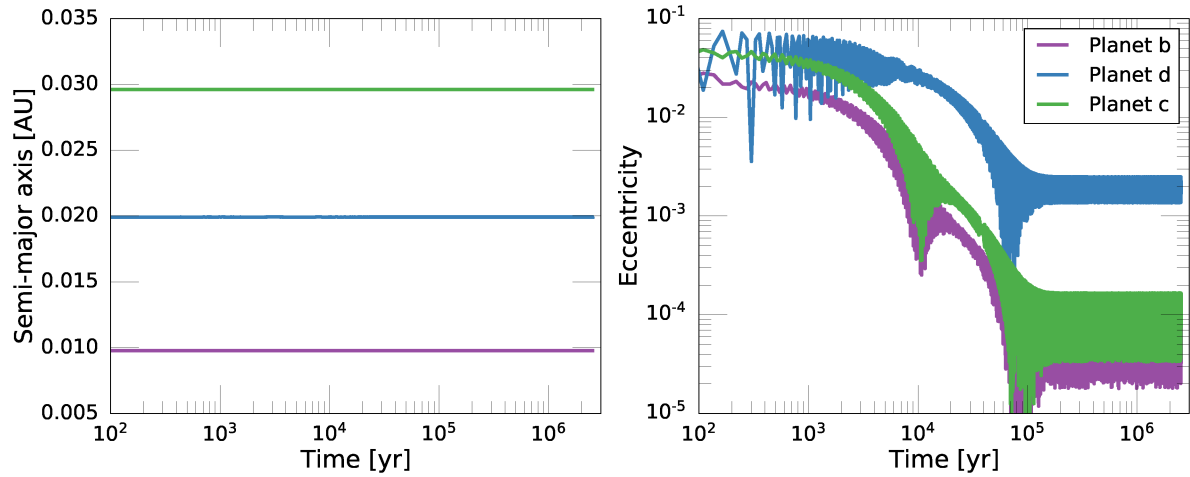
Extended Data Fig. 3 | Damping of free eccentricity in the LP 791-18d system.
a,**b**, Long-term integration for a three-planet system with the observed orbital periods of LP 791-18b, c, and d and initially starting with relatively high free eccentricities (0.02–0.05). The free eccentricities are rapidly damped over a 100,000-year timescale. However, a significant non-zero forced eccentricity circulating between approximately 0.0013 and 0.0025 is preserved for LP 791-18d. The particular simulation shown assumes a tidal quality factor Q_p=100 for all three planets, but even Q_p=1000 will result in a qualitatively similar evolution (see Methods).
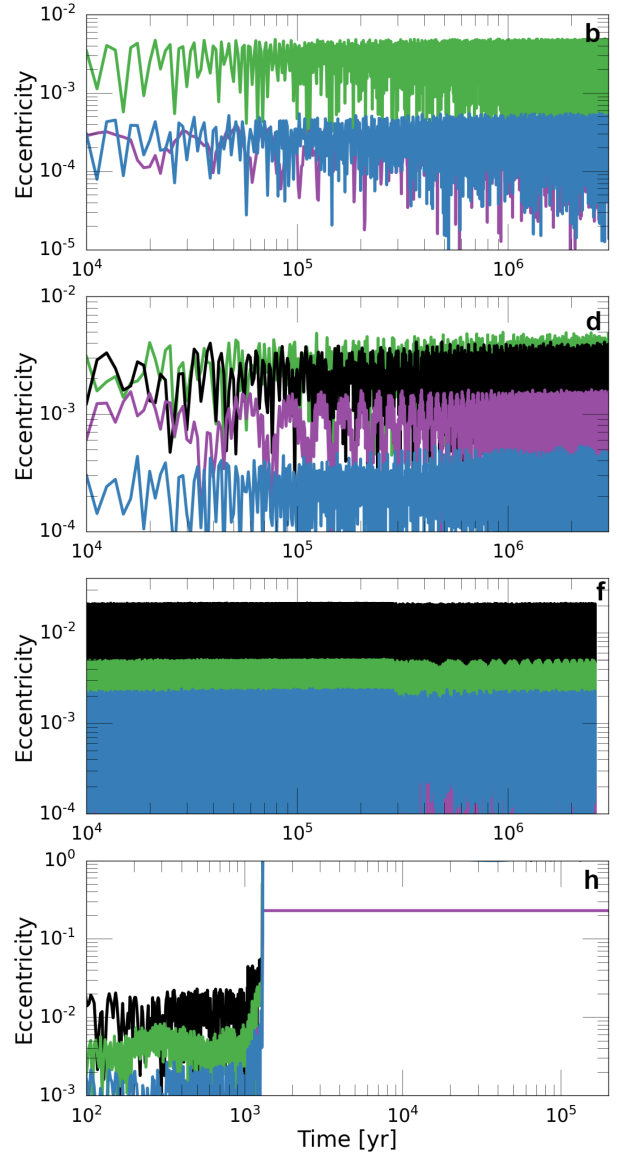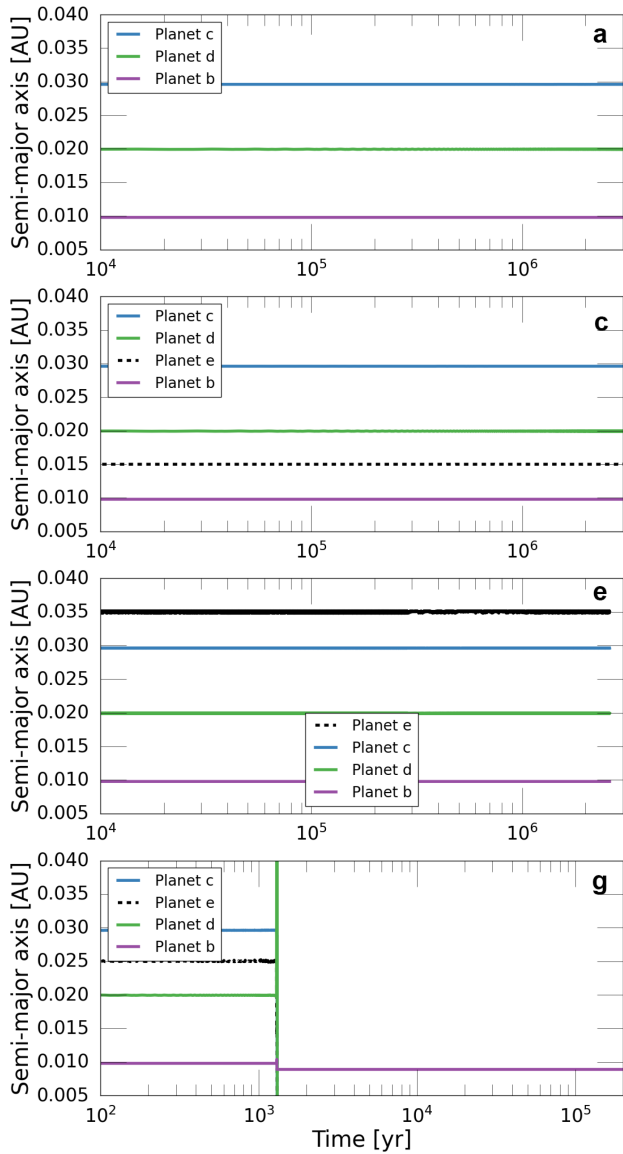
Extended Data Fig. 4 | Dynamical stability analysis of the LP 791-18 system.
a,**b**, Long-term integration for the observed LP 791-18 system, showing that
the system is stable. **c**,**d**, Integration of the LP 791-18 system with an additional
hypothetical 1 M$_\oplus$ planet at 0.015 AU. The system remains long term stable with
this hypothetical planet. **e**,**f**, Integration of LP 791-18 system with an additional
hypothetical 1 M$_\oplus$ planet at 0.035 AU. The system remains long term stable with
this hypothetical planet. **g**,**h**, Integration of LP 791-18 system with an additional
hypothetical 1 M$_\oplus$ planet between planet d and c. The system with this
hypothetical planet quickly becomes unstable.
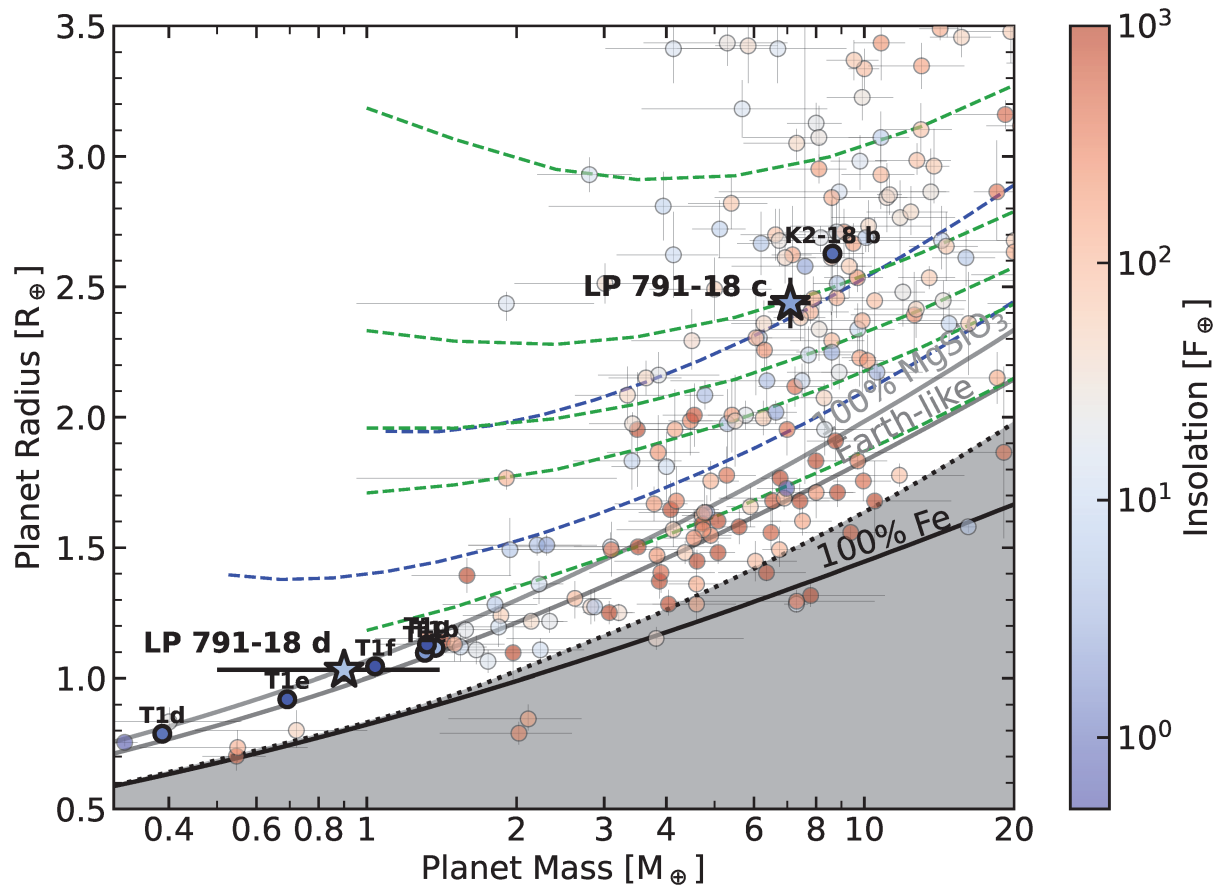
Extended Data Fig. 5 | Mass-radius diagram of small exoplanets. LP 791-18c and d (bold stars) are shown in comparison to other known small planets with measured masses and radii (circles). Horizontal and vertical error bars represent the 68% confidence intervals of the mass and radius measurements for each planet, and the color indicates the planet's stellar insolation. Mass and radius measurements of LP 791-18c and d are reported in this work, while all other measurements are taken from the Exoplanet Archive (https://exoplanetarchive. ipac.caltech.edu). Modeled mass-radius curves are shown for a pure iron composition, an Earth-like composition[91], a pure rocky composition, an Earth-like core with 10% and 50% of the planet's mass composed of a water envelope at $T_{eq}=400K$[10] (dashed blue curves), as well as an Earth-like core with 0.01%, 0.5%, 1%, 2% and 5% of the planet's mass in a H_2/He envelope[9] (dashed green curves). A best match to the mass and radius of LP 791-18c is obtained for Earth-like core with approximately 2% of the planet's mass in a H_2 envelope or, alternatively, approximately 50% of the planet's mass in water. LP 791-18d's composition is consistent with a rocky, potentially Earth-like composition. The TRAPPIST-1 planets and K2-18b are labeled for comparison to LP 791-18d and LP 791-18c, respectively.
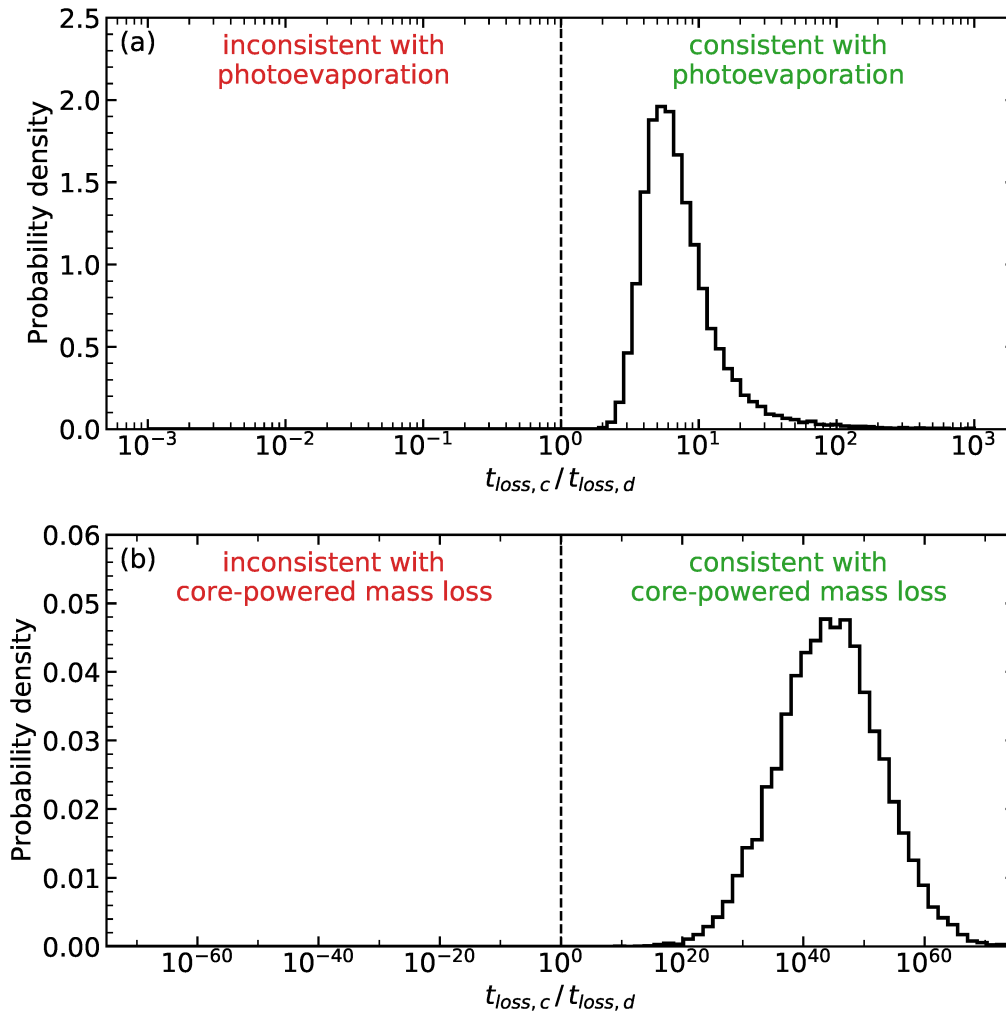
Extended Data Fig. 6 | Mass-loss timescale ratio between LP 791-18c and LP 791-18d under a, the model of photoevaporation[16] and b, the model of core-powered mass loss[16]. Black curves indicate the posterior probability distributions of the mass-loss timescales ratio $t_{loss,c}/t_{loss,d}$ based on simplified scaling laws[12,16], accounting for the observational uncertainties on planet bulk and orbital parameters. The mass-loss timescale of the sub-Neptune LP 791-18c is greater than the mass-loss timescale of the Earth-sized LP 791-18d for all planet masses, radii, and semi-major axes consistent with our observations, indicating that the planet pair is consistent with both the model of photoevaporation and the model of core-powered mass loss.

Extended Data Table 1 | Transit observations of LP 791-18 c

Label	Date	Telescope	Mid-transit time	$+1\sigma$	-1σ	ExoFOP tagid
c1	2019-03-04	TESS	2458546.50940	+0.00109	-0.00117	–
c2	2019-03-08	TESS	2458551.49890	+0.00114	-0.00121	–
c3	2019-03-18	TESS	2458561.47879	+0.00125	-0.00122	–
c4	2019-03-23	TESS	2458566.46952	+0.00147	-0.00131	–
c5	2019-06-16	LCOGT-SSO (Ic)	2458651.29794	+0.00026	-0.00027	18731
c6	2019-10-14	Spitzer (4.5μm)	2458771.05530	+0.00010	-0.00011	–
c7	2019-10-19	Spitzer (4.5μm)	2458776.04491	+0.00011	-0.00010	–
c8	2019-12-13	EDEN-Kuiper 1.5m (I)	2458830.93373	+0.00027	-0.00028	16194
c9	2020-01-27	ExTrA	2458875.84313	+0.00048	-0.00044	–
c10	2020-02-01	ExTrA	2458880.83303	+0.00053	-0.00056	–
c11	2020-02-06	ExTrA	2458885.82335	+0.00034	-0.00037	–
c12	2020-02-11	ExTrA	2458890.81345	+0.00036	-0.00037	–
c13	2020-02-16	EDEN-VATT 1.8m (I)	2458895.80288	+0.00018	-0.00017	17714
c14	2020-02-21	ExTrA	2458900.79250	+0.00042	-0.00040	–
c15	2020-02-26	ExTrA	2458905.78238	+0.00045	-0.00041	–
c16	2020-03-02	ExTrA	2458910.77307	+0.00050	-0.00047	–
c17	2020-03-07	ExTrA	2458915.76215	+0.00058	-0.00058	–
c18	2020-03-12	SPECULOOS South (I+z)	2458920.75273	+0.00035	-0.00035	–
c19	2020-03-12	ExTrA	2458920.75279	+0.00038	-0.00042	–
c20	2020-03-17	ExTrA	2458925.74295	+0.00044	-0.00043	–
c21	2020-03-22	ExTrA	2458930.73283	+0.00046	-0.00039	–
c22	2021-01-05	LCOGT-SSO (I)	2459220.14739	+0.00054	-0.00055	92954
c23	2021-01-10	LCOGT-SSO (I)	2459225.13791	+0.00049	-0.00048	93120
c24	2021-01-15	LCOGT-SSO (I)	2459230.12729	+0.00029	-0.00027	93196
c25	2021-01-25	LCOGT-SSO (I)	2459240.10713	+0.00030	-0.00029	93500
c26	2021-03-11	TESS	2459285.01519	+0.00160	-0.00160	–
c27	2021-03-16	TESS	2459290.00525	+0.00079	-0.00082	–
c28	2021-03-26	TESS	2459299.98501	+0.00096	-0.00100	–
c29	2021-03-31	TESS	2459304.97448	+0.00120	-0.00114	–

Extended Data Table 2 | Transit observations of LP 791-18 d

Label	Date	Telescope	Mid-transit time	$+1\sigma$	-1σ	ExoFOP tagid
d1	2019-03-03	TESS	2458546.38292	+0.00840	-0.00310	–
d2	2019-06-22	SPECULOOS South (I+z)	2458656.51518	+0.00110	-0.00110	–
d3	2019-07-03	SPECULOOS South (I+z)	2458667.52903	+0.00110	-0.00110	–
d4	2019-10-15	Spitzer (4.5μm)	2458772.16042	+0.00049	-0.00038	–
d5	2019-10-18	Spitzer (4.5μm)	2458774.91658	+0.00043	-0.00043	–
d6	2020-02-08	Mearth-S	2458887.80550	+0.00270	-0.00250	16499
d7	2020-02-08	ExTrA	2458887.80760	+0.00150	-0.00160	–
d8	2020-02-08	LCOGT-McD (Ic)	2458887.80957	+0.00113	-0.00188	16479
d9	2020-02-19	TRAPPIST-S (I+z)	2458898.81547	+0.00111	-0.00078	5781
d10	2020-02-19	LCOGT-CTIO (Ic)	2458898.81711	+0.00047	-0.00060	16793
d11	2020-02-19	MEarth-S	2458898.81833	+0.00130	-0.00160	16796
d12	2020-02-19	ExTrA	2458898.81950	+0.00300	-0.00200	–
d13	2020-02-19	LCOGT-CTIO (Ic)	2458898.81956	+0.00056	-0.00061	16944
d14	2020-02-22	MEarth-S	2458901.57132	+0.00140	-0.00150	16848
d15	2020-02-22	LCOGT-SAAO (I)	2458901.57188	+0.00079	-0.00068	16831
d16	2020-02-24	LCOGT-SAAO (I)	2458904.32739	+0.00051	-0.00059	16854
d17	2020-02-24	LCOGT-SAAO (Ic)	2458904.32918	+0.00101	-0.00102	18878
d18	2020-02-27	LCOGT-SSO (Ic)	2458907.08095	+0.00142	-0.00105	16907
d19	2020-03-01	ExTrA	2458909.83300	+0.00350	-0.01120	–
d20	2020-03-01	LCOGT-CTIO (Ic)	2458909.83495	+0.00024	-0.00024	16939
d21	2020-03-01	LCOGT-CTIO (I)	2458909.83498	+0.00042	-0.00036	16957
d22	2020-03-01	MEarth-S	2458909.83580	+0.00090	-0.00100	16954
d23	2020-03-04	LCOGT-CTIO (Ic)	2458912.58695	+0.00071	-0.00055	17294
d24	2020-03-04	MuSCAT2	2458912.58717	+0.00167	-0.00167	–
d25	2020-03-04	TRAPPIST-N (I+z)	2458912.58811	+0.00050	-0.00050	5781
d26	2020-03-04	Mearth-S	2458912.58953	+0.00160	-0.00280	17299
d27	2020-03-12	ExTrA	2458920.84660	+0.00250	-0.00200	–
d28	2020-03-15	ExTrA	2458923.59680	+0.00330	-0.00340	–
d29	2020-03-15	MuSCAT2	2458923.59834	+0.00086	-0.00086	–
d30	2020-03-15	LCOGT-CTIO (Ic)	2458923.59888	+0.00054	-0.00062	18096
d31	2020-03-20	LCOGT-SSO (Ic)	2458929.10736	+0.00081	-0.00089	18176
d32	2020-03-31	LCOGT-SSO (Ic)	2458940.12173	+0.00050	-0.00051	18886
d33	2020-05-11	MuSCAT2	2458981.42173	+0.00175	-0.00175	–
d34	2020-05-28	LCOGT-SSO (Ic)	2458997.94487	+0.00058	-0.00056	19426
d35	2020-12-15	LCOGT-McD (Ic)	2459198.94907	+0.00191	-0.00131	92622
d36	2021-01-09	LCOGT-CTIO (I)	2459223.72737	+0.00312	-0.00106	93100
d37	2021-01-09	ExTrA	2459223.72880	+0.00530	-0.01260	–
d38	2021-01-11	LCOGT-SAAO (I)	2459226.47988	+0.00140	-0.00132	93141
d39	2021-01-14	MuSCAT	2459229.23661	+0.00115	-0.00115	–
d40	2021-01-20	MuSCAT2	2459234.74176	+0.00055	-0.00055	–
d41	2021-01-20	LCOGT-CTIO (I)	2459234.74436	+0.00079	-0.00279	93449
d42	2021-02-03	LCOGT-CTIO (I)	2459248.50750	+0.00210	-0.00210	–
d43	2021-02-25	MuSCAT2	2459270.53282	+0.00081	-0.00081	–

Extended Data Table 3 | Stellar parameters of LP 791-18

Parameter	Value	Source
Identifying Information		
TIC ID	181804752	TIC v8
α R.A. (hh:mm:ss)	11:02:45.709	*Gaia* eDR3
δ Decl. (dd:mm:ss)	-16:24:23.23	*Gaia* eDR3
Epoch (year)	2016.0	*Gaia* eDR3
$\mu_\alpha \cos\delta$ (mas yr^{-1})	-221.29 ± 0.04	*Gaia* eDR3
μ_δ (mas yr^{-1})	-58.84 ± 0.04	*Gaia* eDR3
Distance (pc)	26.65 ± 0.03	*Gaia* eDR3
Photometric Properties		
V (mag)	16.9 ± 0.2	TIC v8
G (mag)	15.0715 ± 0.0013	*Gaia* DR2
G_{BP} (mag)	17.23831 ± 0.072	*Gaia* DR2
G_{RP} (mag)	13.69512 ± 0.0029	*Gaia* DR2
u (mag)	21.28 ± 0.14	SDSS
g (mag)	17.8827 ± 0.0057	SDSS
r (mag)	16.2672 ± 0.0039	SDSS
i (mag)	14.3142 ± 0.0035	SDSS
z (mag)	13.2565 ± 0.0035	SDSS
J (mag)	11.559 ± 0.024	2MASS
H (mag)	10.993 ± 0.022	2MASS
K_S (mag)	10.644 ± 0.023	2MASS
$W1$ (mag)	10.426 ± 0.023	AllWISE
$W2$ (mag)	10.233 ± 0.21	AllWISE
$W3$ (mag)	10.024 ± 0.062	AllWISE
Spectroscopic and Derived Properties		
Spectral Type	M(6.1 ± 0.7)V	[4]
Barycentric RV (km s^{-1})	$+14.1 \pm 0.3$	"
Age (Gyr)	> 0.5	"
[Fe/H]	-0.09 ± 0.19	"
T_{eff}	2960 ± 55	"
$\log_{10} g$ (cgs)	5.115 ± 0.094	"
$v \sin i$	< 2	"
$M_* (M_\odot)$	0.139 ± 0.005	"
$R_* (R_\odot)$	0.182 ± 0.007	This paper
$\rho_* (\rho_\odot)$	$23.06^{+3.02}_{-2.59}$	This paper
$L_* (L_\odot)$	0.00230 ± 0.00001	This paper
ld_0 TESS	0.26 ± 0.06	[4]
ld_1 TESS	0.55 ± 0.07	"
ld_0 *Spitzer* 4.5μm	$0.043^{+0.062}_{-0.038}$	This paper
ld_1 *Spitzer* 4.5μm	$0.099^{+0.114}_{-0.071}$	"
ld_0 LCOGT	0.34 ± 0.02	"
ld_1 LCOGT	0.40 ± 0.03	"
ld_0 MEarth	0.33 ± 0.02	"
ld_1 MEarth	0.38 ± 0.03	"
ld_0 TRAPPIST	0.26 ± 0.01	"
ld_1 TRAPPIST	0.33 ± 0.02	"

Extended Data Table 4 | Planet parameters

Parameter	Units	b	c	d
T_0	$\text{BJD}_{\text{TBD}} - 2457000$	$2458774.86973^{+0.00018}_{-0.00018}$	$2458771.055182^{+0.000091}_{-0.000097}$	$2458772.16211^{+0.00050}_{-0.00082}$
P	day	$0.9479981^{+0.0000021}_{-0.0000021}$	$4.9899093^{+0.0000074}_{-0.0000072}$	$2.753436^{+0.000013}_{-0.000013}$
R_p/R_*	-	$0.0610^{+0.0018}_{-0.0018}$	$0.12261^{+0.00097}_{-0.00097}$	$0.05192^{+0.00090}_{-0.00090}$
R_p	$R_\oplus$	$1.212^{+0.059}_{-0.058}$	$2.438^{+0.096}_{-0.096}$	$1.032^{+0.044}_{-0.043}$
Mass	$M_\oplus$	-	$7.1^{+0.7}_{-0.7}$	$0.9^{+0.5}_{-0.4}$
a	AU	$0.00978^{+0.00012}_{-0.00012}$	$0.02961^{+0.00035}_{-0.00036}$	$0.01992^{+0.00024}_{-0.00024}$
e	-	-	$0.00008^{+0.00004}_{-0.00004}$	$0.0015^{+0.00014}_{-0.00014}$
b	-	$0.33^{+0.19}_{-0.19}$	$0.134^{+0.082}_{-0.082}$	$0.27^{+0.17}_{-0.17}$
i	degrees	$88.37^{+0.94}_{-0.95}$	$89.78^{+0.13}_{-0.13}$	$89.34^{+0.41}_{-0.41}$
T_{14}	minutes	$37.17^{+0.52}_{-0.52}$	$70.03^{+0.51}_{-0.51}$	$54.91^{+1.50}_{-1.51}$
S_{inc}	$S_\oplus$	$24.14^{+0.61}_{-0.57}$	$2.637^{+0.066}_{-0.062}$	$5.83^{+0.15}_{-0.14}$
T_{eq} [1]	K	$564.3^{+3.5}_{-3.4}$	$324.4^{+2.0}_{-1.9}$	$395.5^{+2.6}_{-2.3}$
$K_{\text{RV,predicted}}$	m/s	4.4 [2]	$9.9^{+1.0}_{-1.0}$	$1.53^{+0.85}_{-0.68}$

[1]Assuming an Earth-like albedo of Ab=0.3 and uniform heat redistribution. [2]Prediction of RV semi-amplitude of Planet b is based on empirical mass-radius relationship.